NTNU – Trondheim
Norwegian University of
Science and Technology

Softening Behaviour of Selected Commercially Pure Aluminium Model Alloys

Gunnar Sande

Materials Science and Engineering
Submission date: June 2012
Supervisor: Knut Marthinsen, IMTE
Co-supervisor: Sindre Bunkholt, IMTE

Norwegian University of Science and Technology
Department of Materials Science and Engineering

Declaration

I hereby confirm that this work has been done independently and in accordance with the laws of the Master of Science in Architecture and Engineering exam at the Norwegian University of Science and Technology (NTNU).

Trondheim, 15 June 2012

_____

Gunnar Sande

Preface

This master's thesis is the result of work done at the Department of Materials Science and Engineering at NTNU during spring 2012. The work is closely related to the MOREAL project, a collaboration between NTNU, Sintef, Hydro Aluminium and Sapa. The goal for this project is to make better aluminium alloys from recycled sources through numerical modelling. The models has to be based on comprehensive experimental work on relevant alloys for improved understanding and a quantitative description of the phenomena involved, and the present work is a contribution to this latter objective.

First I would like to thank my supervisor Professor Knut Marthinsen who has given good help and guidance throughout my work. Phd candidate Sindre Bunkholt has contributed greatly and deserves special thanks. I would also like to thank Pål Ulseth, Erlend Nordstrand, Yingda Yu, Wilhelm Dall and Gavin Wang for their help with my experimental work.

Abstract

A characterization of the softening behaviour of four different commercially pure aluminium alloys has been carried out. The work is related to the MOREAL project (Modelling towards value-added recycling friendly aluminium alloys), where the main goal is to quantify the effect of the elements in recyclable aluminium alloys on microstructure and mechanical properties during thermo-mechanical processing. Typical elements are iron (Fe), silicon (Si) and manganese (Mn), and the alloys studied in this work contain Fe and Si with different amount and ratio:

Name	*Fe* [wt%]	*Si* [wt%]	*Al*
A1	0.15	0.05	Balance
A2	0.15	0.15	Balance
B1	0.5	0.05	Balance
B2	0.5	0.15	Balance

The as-cast material of all four alloys were homogenized at 600 °C for 24 hours followed by a cooling sequence to 450 °C, implying a total dwell time of 160 hours. The alloys were then cold rolled to a strain of 2.6 and isothermally annealed at temperatures from 275 °C to 375 °C, and the physical and mechanical properties were followed with electrical conductivity and hardness measurements. The microstructure and texture has been investigated with electron backscattering diffraction (EBSD) in scanning electron microscope (SEM), optical light microscopy and orientation distribution functions (ODF) from X-ray diffraction.

Alloy A1 and A2 where fully recrystallzed after 10^4 seconds when isothermally annealed at 300 °C. Alloy B1 and B2 are slightly faster to reach the fully recrystallized state than alloy A1 and A2. The decrease in mechanical properties during softening was nearly linear on a logarithmic time scale, especially for alloy B1 and B2, with the onset of recrystallization difficult to seperate from the recovery. Electrical conductivity measurements showed that there was minimal concurrent precipitation. Images of the microstructure of the samples annealed at 275 °C show a long recovery phase followed by recrystallization. Particle stimulated nucleation (PSN) sites seems to be an important nucleation mechanism as it is found that the initial grain size have little effect on the softening kinetics, indicating that nucleation on old grain boundaries is of little importance. The recrystallization texture is weak with the typical cube orientation slightly rotated around the normal direction. The recrystallized grain size was found to be smaller in alloy B1 and B2 (16-20 μm) than in alloy A1 and A2 (21-27 μm), most likely due to more PSN sites in these alloys. The grain growth that followed after recrystallization was found to be slightly larger for alloy A1 and A2 than alloy B1 and B2, most likely due to lower solute drag.

Sammendrag

En karakterisering av avfastningsforløpet til fire ulike kommersielle ren-aluminiumslegeringer har blitt gjennomført. Arbeidet er knyttet til MOREAL-prosjektet (Modelling towards value-added recycling friendly aluminium alloys), hvor målsetningen er å kvantifisere effekten elementene i resirkulerbare aluminiumslegeringer har på mikrostruktur og mekaniske egenskaper under termo-mekanisk bearbeiding. Typiske elementer er jern (Fe), silisium (Si) og mangan (Mn), og legeringene studert i dette arbeidet inneholder Fe og Si i ulik mengde og forhold:

Navn	*Fe* [vekt%]	*Si* [vekt%]	*Al*
A1	0.15	0.05	Balanser
A2	0.15	0.15	Balanser
B1	0.5	0.05	Balanser
B2	0.5	0.15	Balanser

Alle fire legeringene ble i som-støpt tilstand homogenisert på 600 °C i 24 timer, etterfulgt av en nedkjølingssekvens til 450 °C, noe som medførte en holdetid på totalt 160 timer. Legeringene ble deretter kaldvalset til en tøyning på 2.6 og isotermt tilbakeglødet på temperaturer fra 275 °C til 375 °C, og de fysiske og mekaniske egenskapene har blitt fulgt med målinger av elektrisk ledningsevne og hardhet. Mikrostrukturen og teksturen har blitt undersøkt med EBSD-teknikken (electron backscattering diffraction) i elektronmikroskopet, lysmikroskop og ODF-er (orientation distribution function) fra røntgendiffraksjon.

Legering A1 og A2 var fullstendig rekrystallisert etter 10^4 sekunder når den ble tilbakeglødet isotermt på 300 °C. Legering B1 og B2 ble fullstendig rekrystallisert noe raskere enn legering A1 og A2. Mekaniske egenskaper under tilbakegløding viste en nær lineær nedgang på en logaritmisk tidsskala, spesielt legering B1 og B2, og starttidspunktet for rekrystallisasjon var vanskelig å skille fra gjenvinningsfasen. Målingene av elektrisk ledningsevne viste at det var minimalt med samtidig presipitering. Mikrostrukturbilder av prøvene glødet på 275 °C viser en langsom gjenvinningsfase med etterfølgende rekrystallisasjon. Det virker som PSN-punkter (particle stimulated nucleation) er en viktig kimdanningsmekanisme, ettersom det ble funnet ut at den opprinnelige kornstørrelsen har liten effekt på avfastningskinetikken, noe som indikerer at det er lite kimdanning på gamle korngrenser. Rekrystallisasjonsteksturen var svak med kube-orienteringen noe rotert rundt prøvenormalen. Rekrystallisert kornstørrelse var mindre i legeringene B1 og B2 (16-20 μm) enn i legeringne A1 og A2 (21-27 μm), mest sannsynlig på grunn av flere PSN-punkter. Kornveksten som etterfulgte rekrystallisasjon ble funnet til å være noe større i legeringne A1 og A2 enn i legeringene B1 og B2, mest sannsynlig på grunn av færre løste legeringselementer.

Contents

1 Introduction

A long term vision of the Norwegian aluminium industry is to be world leading with respect to sustainability and competitiveness. The primary aluminium production is gradually being driven out of Europe due to higher energy cost, environmental regulations and competitons from emerging economies. To meet these challenges and to have a sustainable development, the Norwegian aluminium industry must provide the best quality products of both primary-based and recycle-based aluminium at a competitve price.

By using recycled aluminium, only 5% of the energy compared to production from primary sources is needed. However, the changes and variations in the composition (alloying elements and impurities) is a challenge. To handle this and be able to deliver taylor-made high quality recycle based alloys, optimization of the thermo-mechanical processing routes is needed. Traditional trials and experiments can be both costly and time consuming. Advanced mathematical modelling tools, as a complementation to traditional experimental research, is beleived to be a powerful tool towards better and more intelligent alloy design and and material processing strategies. To be able to use and trust the models, they must be based on a comprehensive and detailed characterization of the roles of alloying elements and impurities.

This is the basis of the MOREAL project (Modelling towards value-added recycling friendly aluminium alloys), a collaboration between NTNU, Sintef, Hydro Aluminium and Sapa. Its objective is to develop physically based numerical models to predict the microstructure evolution through homogenization, deformation and annealing, as well as the mechanical properties.

The present work is a part of a characterization of the softening behaviour of the alloys for which the Alsoft model should be applicable. Alsoft is a softening model that calculates the microstructure evolution from deformed to softened material, i.e. the processes known as recovery, recrystallization and grain growth. From these calculations it gives the mechanical properties to the material through appropriate microstruture relationships.

The softening mechanisms belong to one of the least understood phenomena in metallurgy because they represent irreversible thermodynamic transitions rather than equilibrium phase transformations. The current understanding was developed in the late 80th and 90th century and has already been applied by the Norwegian aluminium industry. However, crucial aspects like nucleation of recrystallization, concurrent precipitation and more complex thermo-mechanical treatments are not sufficiently understood or quntitatively described.

The work presented in this report is the characterization of softening behaviour of alloys containing small additions of iron (Fe) and silicon (Si). These elements are present in all aluminium alloys, and have a tendency of accumulating during repeated recycling. The effect of the total amount of alloying elements and the Fe/Si ratio are studied with respect to softening kinetics, physical and mechanical properties, recrystallized grain size, grain growth and texture evolution.

2 Theory

Aluminium (Al) alloys are divided into two groups with respect to hardenabiliy; heat treatable and non-heat treatable. Commercially pure aluminium (denoted AA1xxx), which is more than 99% Al with small additions of Fe and Si, is a non-heat treatable alloy. Its strength is due to elements in solid solution and strain hardening, and second phase particles will only to some extent contribute with a hardening effect. Important aspects of the process route relevant for the present work and its influence on the microstructure of the material is presented in the this chapter.

2.1 Processing route

A typical production route for aluminium sheets is given in Figure 2.1. Processing a non-heat treatable aluminium alloy involves several steps to obtain the desired properties. After casting, most alloys are heat treated, mainly to remove microsegregation, i.e. to get an even particle structure and an uniform microstructure. This is often referred to as homogenization. Usually, the material is then passed through a hot rolling mill where the thickness is reduced. The strip from the hot mill is cooled before cold rolling where the thickness is further reduced. The rolling of the material to sheets introduces large strains which makes the material hard and difficult to form. It is often necessary with annealing to increase ductility for further processing. The processes of cold rolling and annealing is relevant for this work, and will be presented in the next sections.

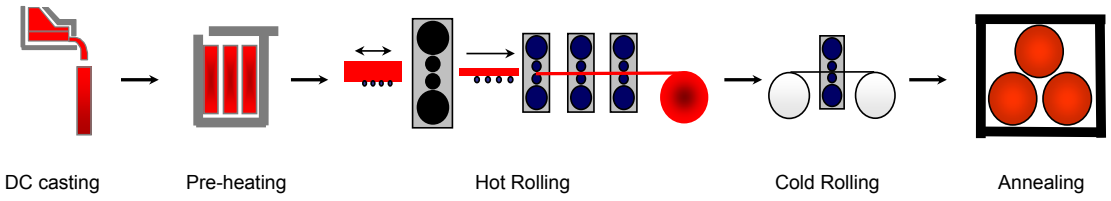

Figure 2.1: An example of the typical production steps for rolled aluminium products.

2.2 Cold rolling

Cold rolling is the process of plastically deforming metal by passing it between rolls. The energy which does not result in heat is stored in the material as defects, as the lattice is distorted during deformation. The typical deformed microstructure consists of elongated grains and there is a large increase in the total grain boundary area. The defects are in particular dislocations, as point defects anneal out at low temperatures and and have little effect on mechanical properties. The increase in stored energy is the driving pressure for the reactions which takes place on subsequent annealing, like recovery and recrystallization.

During cold rolling to medium and large strains, a typical deformation structure consisting of subgrains, and dislocations will develop, illustrated in Figure 2.2a. The dislocations in the deformed material is described with the dislocation density within the

subgrains (ρ_i) and the dislocations which are arranged in subgrains, characterized with the subgrain size (δ) and misorientation between subgrain boundaries (θ). For lower strains, the number of dislocations within the subgrains is related to the subgrain size by the principle of similitude: $\delta \cdot \sqrt{\rho_i} =$ constant [1]. Work done on several Al alloys shows that the dislocation density saturates at a strain larger than 2 [2].

2.3 Annealing of deformed material

Annealing is a heat treatment, and the thermal energy gives the dislocations oppurtunity to annihilate or move to a configuration with lower energy. This configuration is a substructure which usually does not affect the boundaries between the deformed grains. This is called recovery and the microstructure during this process is illustrated in Figure 2.2a. Even though the amount of residual stresses decrease, there are only little changes in the mechanical properties as the dislocation density remains more or less unchanged. The yield stress will decrease slightly at beginning of the annealing time, as shown schematically in Figure 2.3. One of the most important parameters determining the rate of recovery in metals and alloys is the stacking fault energy (γ_{SFE}). Aluminium is a metal of high stacking fault energy which means that dislocation climb is fast, and significant recovery may occur.

As the dislocations represent stored energy, the substructure is a metastable state and further annealing may result in nucleation of new dislocation-free grains within the deformed or recovered structure. This is called recrystallization and is illustrated in Figure 2.2c. The new grain structure grows and the old grains are eliminated. The new structure has a low dislocation density, and the mechanical properties will change considerably, as indicated with the large drop in yield stress in Figure 2.3. The combined process of recovery and recrystallization are often referred to as softening. Several factors that affect recrystallization will later be presented.

A fully recrystallized material (Figure 2.2d) will still be thermally unstable as it contains grain boundaries. Further annealing may result in grain growth, where the large grains grow at the expense of the small ones, see Figure 2.2e. Abnormal grain growth may occur in certain circumstances, where only a few selected large grains starts to grow, and a bi-modal grain size distribution develops, see Figure 2.2f. The pinning of subgrain and grain boundaries by solutes and second-phase particles is an important factor affecting bot recovery, recrystallization and grain growth.

2.3.1 Precipitation

Precipiates are a very important factor to consider when studying annealing, and some general aspects concerning this will be presented. Nucleation and growth of a precipitate from a supersaturated solid solution is controlled by the thermodynamic concept of free energy minimization. The supersaturated material is in a metastable state, and an activation energy is needed for the reaction to start. If the interface between the precipiate and the matrix is seperated by a phase boundary (incoherent particles), the growth rate is determined by both diffusion and the jump frequency of atoms across the

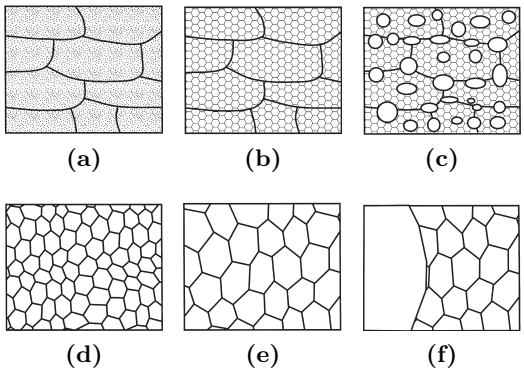

Figure 2.2: Illustration of the evolution of microstructure during annealing, from deformed state (a) through recovery (b), recrystallization (c-d), grain growth (e) and abnormal grain growth (f) [3].

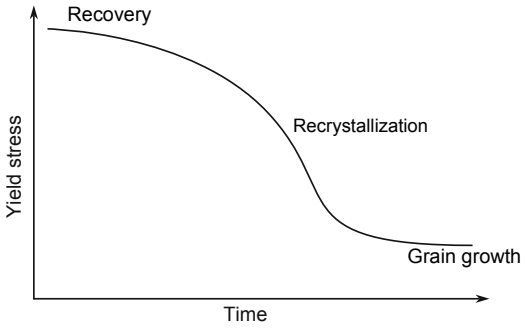

Figure 2.3: The yield stress againt time for a typical annealing process. Moderate decrease at the beginning during recovery, while a large decrease during recrystallisation.

boundary. The interface of fully coherent particles have low mobility and the growth is usually diffusion controlled.

Precipitates have a large effect on the softening behaviour. If the precipitates are small, they interact with the moving grain boundaries with a retarding pressure called the Zener drag [4]. The processes of recovery, recrystallization and grain growth are therefore generally slowed down by precipitates. This is the reason why precipitiation is important to consider when studying the softening behaviour. Under some circumstances, if the density of the precipitates is high, the recrystallization may be stagnated and the restoration of the microstructure occurs by what is called extended recovery. In this case, the subgrain structure grows and the kinetics are controlled by the coarsening of the particles.

The effect of the Zener drag depends on the interface, shape, size, spacing and volume fraction of the particles. The force acting on a moving boundary is maximum when it meets the particle at a 45° angle (see Figure 2.4a), and is given by [3]:

$$F_Z = \pi r \gamma_{GB}, \tag{2.1}$$

where r is the radius of the particle and γ_{GB} is the grain boundary energy. The force from a distribution of particles can be calculated by taking the number of particles per unit volume (N_V) and the volume fraction (f_r) of randomly distributed particles of average size r into account, which is given by:

$$N_V = \frac{3f_r}{4\pi r^3} \tag{2.2}$$

If the boundary is planar, then particles within a distance r on either side of the boundary will intersect it. Therefore the number of particles intersecting unit area of the boundary is:

$$N_S = 2rN_V = \frac{3f_r}{2\pi r^2} \tag{2.3}$$

The pinning pressure (P_Z) exerted by the particles per unit area boundary is expressed by combining this equation with the maximum force:

$$P_Z = N_S \cdot F_Z = \frac{3f_r\gamma_{GB}}{2r} \tag{2.4}$$

From this it is seen that small and many particles will give a large Zener drag, while few and large will give a lower or insignificant Zener drag.

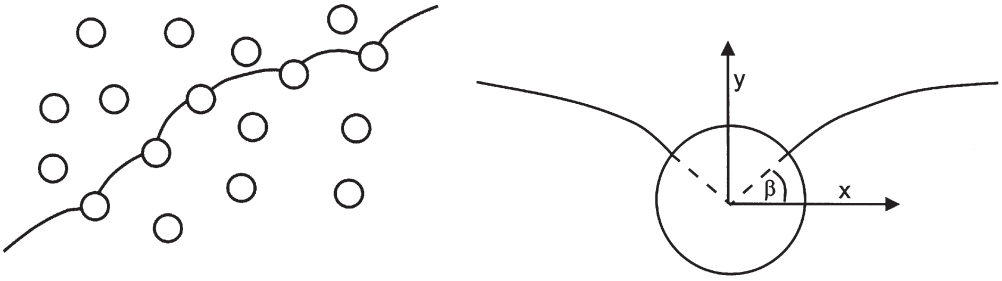

(a) Interactions between particles and a grain boundary. **(b) Maximum force when β=45°.**

Figure 2.4: Illustration of the effect of particles on grain boundaries [3].

Precipitation during annealing, called concurrent precipitation, may happen for supersaturated metals which are deformed and annealed. This will affect both the subgrain growth and the growth of recrystallized grains [5]. Precipitation requires a certain period of time and will in many cases mainly occur after recrystallization is finished for materials with low supersaturated alloying elements, and its effect will be limited. At the lowest temperatures however, the driving force for precipiation is usually higher than at the higher temperatures due to lower solubility of alloying elements, and precipitation will start earlier. For low temperatures and long annealing times, precipitation may thus occur prior to and postpone the start of recrystallization.

2.3.2 The effect of alloying elements

Iron The solubility of Fe in Al is very low, and the limit at different temperatures is given in Figure 2.5a [6, 7]. However, it has been found that even small differences in Fe in solid solution has an effect on the softening behaviour. Softening of aluminium with 0.02 wt% Fe in solid solution was shifted towards significantly longer annealing times compared to aluminium with 0.01 wt% Fe in solid solution [8]. After investigating alloys with low Fe content in supersaturated solution (up to 0.04 wt%), it was found that the resulting texture existed of the cube and the R texture components, with the R orientation more dominating as the Fe content increase [9]. If Fe was strongly precipitated, retained rolling texture dominated, with no cube orientations present.

Silicon The solid solubility of Si is much higher than the solubility of Fe, at around 1.44 wt% at the eutectic temperature, see Figure 2.5b [10]. Si in supersaturated solid solution is therefore common and may be subject to precipitaion during annealing.

Work done on alloys with 0.61 wt% Fe and 0.16 wt% Si shows that precipiation of Al_3Fe mainly occurs after the completion of recrystallization. Si has a small effect on the softening behaviour both as particles and in solid solution, but will has an effect in combination with Fe in the form of AlFeSi particles. Precipitation of Si occurs during annealing and is accelerated by cold rolling as the dislocations acts as nuclei. [11]

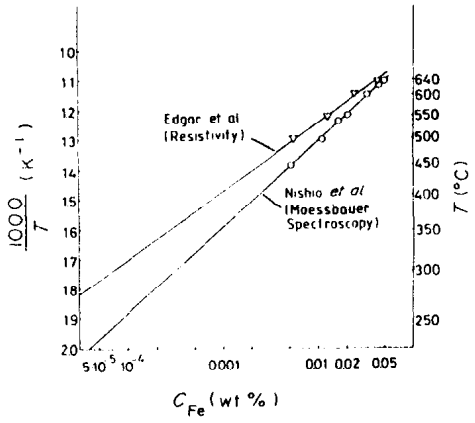

(a) Solubility limit for Fe in Al [6, 7].

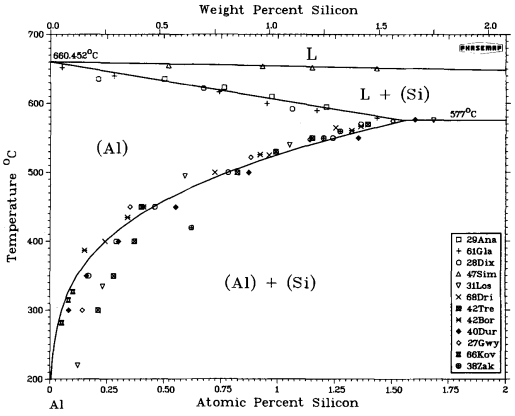

(b) Al-Si phase diagram with the Al-rich solidus and experimental data [10].

Figure 2.5: The solid solubility of Fe and Si can be seen in these diagrams.

2.4 Modelling softening behaviour

A particular computer model capable of calculating the softening behaviour of aluminium alloys is called Alsoft and is based on the work by Vatne et al. [12]. The basic theory and the fundamental expressions for this model will be presented in this section.

The classic approach to model the kinetics of recrystallization is to use this equation for fraction recrystallized (X):

$$X(t) = 1 - \exp[-X_{ext}(t)], \tag{2.5}$$

where X_{ext} is the extended volume fraction, i.e. the volume fraction one would get by not taking into account that the already recrystallized grains overlaps. A main assumption is the random spatial distribution of nucleation sites. A more general explicit analytical expression for further applications is given by the the Jonhson–Mehl–Avrami–Kolmogorov (JMAK) equation, which gives fraction recrystallized by [13, 14, 15]:

$$X(t) = 1 - \exp(-kt^n), \tag{2.6}$$

where k is a constant and n is the Avrami exponent, parameters which is commonly used to characterize recrystallization kinetics. Expressions of this kind is only possible in highly idealized cases, and one of these conditions is the so-called "site saturation" kinetics (n=3), where a given number of nuclei starts to grow at the same time (usually t=0) with a constant growth rate. The corresponding case where a constant nucleation rate is assumed is called "Johnson Mehl" (n=4).

2.4.1 Recovery kinetics

The recovery of dislocations due to subgrain growth can be expressed by the time dependence of the average distance between each dislocation (r):

$$\frac{dr}{dt} = C_1 v, \tag{2.7}$$

where C_1 is a constant found experimentally and v is the dislocation density. A general expression for the dislocation velocity is given as [16]:

$$v = \nu_D b B_\rho \exp\left(-\frac{U_a}{kT}\right) 2\sinh\left(\frac{Fb^2}{kT}\right), \tag{2.8}$$

where ν_D is a frequency term, U_a is the activation energy, B_ρ is a constant and F is the force on the dislocation per unit length. This experssion is valid for all F, which can be derived from the change in free energy associated with the decrease in dislocation density ρ_i:

$$F = A_\rho G b^3 \sqrt{\rho_i}, \tag{2.9}$$

where A_ρ is a constant taking care of the effect from solute drag, G is the shear modulus and b is Burgers vector. The dislocations arranged within subgrains is in Alsoft treated for themselves and their kintetics may be modelled similar to the dislocation density [8]. Alsoft uses the following equation to calculate dislocation density (ρ_i) and subgrain growth (δ):

$$\dot{\rho}_i(t) = -\nu_D b A_\rho B_\rho \rho(t)^{3/2} \exp\left(-\frac{U_a}{RT(t)}\right) 2\sinh\left(\frac{A_\rho G b^4}{kT(t)}\sqrt{\rho_i(t)}\right) \tag{2.10}$$

$$\dot{\delta}(t) = \nu_D b A_\delta B_\delta \exp\left(-\frac{U_a}{RT(t)}\right) 2\sinh\left(\frac{A_\delta G b^4}{kT(t)}\frac{1}{\delta(t)}\right) \tag{2.11}$$

2.4.2 Recrystallization kinetics

The equations used to calculate the growth of recrystallized grains is given in this section. In the simplified case of site saturation, the extended volume fraction is given by following expression:

$$X_{ext} = \frac{4}{3}\pi N (Gt)^3, \tag{2.12}$$

where N is the total number of nuclei and G is the growth rate given by:

$$G(t) = M(P_D - P_Z), \tag{2.13}$$

where M is the mobility of the new grain boundaries and P_D is stored energy which is the energy introduced during deformation and the driving force for recovery and recrystallization. The mobililty of the grain boundaries is given as:

$$M = \frac{M_0}{c_{ss} RT} \exp\left(-\frac{U_{GB}}{RT}\right) \tag{2.14}$$

As seen, the mobility is strongly dependent on the temperature T, as well as the activation energy for grain boundary mobility U_{GB} and the material constant M_0. Note that the mobility decreases as the level of solid solution c_{ss} increases.

A nuclei must be thermodynamically stable in order to grow. The critical size for successful nucleation ($\delta^*(t)$) is given by the Gibbs–Thompson relationship:

$$\delta^*(t) = \frac{2\gamma_{GB}}{P_D - P_Z}, \tag{2.15}$$

where γ_{GB} is the grain boundary energy between the nuclei and the matrix and $P_D - P_Z$ is the effective stored energy. The stored energy (P_D) is derived from the dislocations generated during deformation in the interior of subgrains (ρ_i), those which makes up the subgrains (δ) and the boundary energy (γ_{SB}):

$$P_D = \frac{Gb^2}{2}\rho_i + \alpha\frac{\gamma_{SB}}{\delta} \tag{2.16}$$

Here, G is the shear modulus and α is a geometrical constant (~ 3 in an equiaxed substructue). Another important factor is the misorientation between the subgrains (θ) and is used to calculate stored energy (γ_{SB}) by the Read–Shockley relation:

$$\gamma_{SB} = \frac{Gb\theta}{4\pi(1-\nu)}\left(1 - \ln\frac{\theta_c}{\theta}\right), \tag{2.17}$$

where ν is the Poisson ratio and θ_c is the critical misorientaion seperating the high angle and the low angle grain boundaries.

2.4.3 Nucleation sites of recrystallization grains

Nucleation of recrystallization is not possible through "classical" nucleation, i.e. through a stochastic process, and the recrystallized grains develop from regions already existing in the deformed state [17]. Moreover, any potential nuclei must posess a mobile high angle grain boundary to grow. Grain boundaries with misorientation greater than a certain angle, typically between 10° and 15°, are called high angle grain boundaries (HAGB), and those with misorientations less than this are called low angle grain boundaries (LAGB). Since HAGBs generally do not exist in the subgrain structure [8], nucleation is restricted to nucleation sites where local misorientaions can develop. These are presented here:

Particle stimulated nucleation (PSN) PSN is a generally accepted nucleation mechanism in aluminium alloys and is regarded as the most usual in alloys containing large (>1 μm) undeformable particles [18]. The nucleation takes place in the deformation zone around the particle, as illustrated in Figure 2.6. The number of potential nuclei can therefore be altered by alloying elements and processing to produce large particles acting as nucleation sites, and grain size and recrystallization texture may be controlled by the amount of PSN.

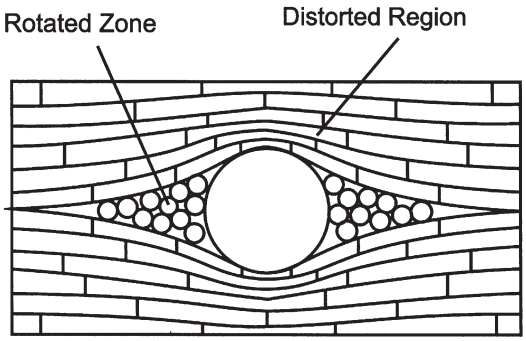

Figure 2.6: The deformation zone around a particle [3].

Cube An important texture component and nucleation mechanism in several aluminium alloys is the cube sites. The cube orientation which survives the deformation gets a band-like shape called cube bands, which surface may act as nucleation sites (see Figure 2.7) [19, 20, 12]. The cube oriented subgrains are very effective as nucleation sites, partly due to a certain size advantage and partly due to their growth advantage. Their growth efficiency seems to be due to their 40°<111> orientation to the adjacent S components after deformation, which is a very common rolling texture component in rolled aluminium (more explaination of textures is in Chapter 2.5). The grains with 40°<111> orientation relationship to their neighbours possess the the largest growth rates. A lot of work have been done on the origin of the strong cube texture in aluminium, and it is still debated.

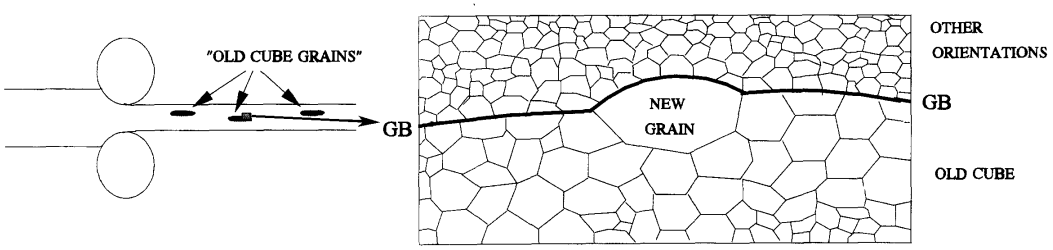

Figure 2.7: Illustration of the nucleation mechanism of recrystallized cube grains from deformed cube bands [12].

Grain boundary nucleation Grain boundary nucleation is in general a nucleation mechanism as different stored energies and subgrain sizes may exist across an "old" grain boundary. Combined with the already existing large misorientaion, grain boundaris provides good conditions for growth. The cube nucleation mechanism is only a special case of grain boundary nucleation.

2.4.4 Grain growth kinetics

Burke and Turnbull analysed the grain growth kinetics based on that the driving pressure (P) on a boundary arises from the curvature of the boundary [21, 22]. If the R_1 and R_2 are the principial radii of curvature of the boundary of energy γ_{GB}, the driving pressure is given by:

$$P = \gamma_{GB}\left(\frac{1}{R_1} + \frac{1}{R_2}\right) \tag{2.18}$$

If it is further assumed that the grain boundary energy is the same for all boundaries, the boundaries are all part of spheres and the radius of curvature (R) is proportional to the mean radius of an individual grain ($\overline{R}$), the driving pressure can be expressed as:

$$P = \frac{\alpha\gamma_{GB}}{\overline{R}} \tag{2.19}$$

where α is a geometrical constant. If the boundary velocity (dR/dt) is assumed to be proportional to the driving pressure with a constant c, the following general expression may be derived:

$$\overline{R}^n - \overline{R_0}^n = ct \tag{2.20}$$

This equation is called the parabolic growth law. The constant n is often termed the grain growth exponent and is found experimentally to be above 2 in many cases. For high purity aluminium it is often found to be 4 [23]. If second-phase particles are present, the pinning pressure (P_Z) must be incorporated and the rate of grain growth in this model becomes:

$$\frac{dR}{dt} = M(P - P_Z) = M\left(\frac{\alpha\gamma_{GB}}{\overline{R}} - \frac{3f_r\gamma_{GB}}{2r}\right) \tag{2.21}$$

From this equation, it can be seen that grain growth will cease when $P = P_Z$. If there is sufficient amount of particles, and a limiting grain size would be reached. In special cases, the Zener pressure may be large enough to totally prevent recrystallization, as seen from Equation 2.15.

2.5 Texture

Texture is the preferred orientation of the grains in an polycrystalline material, and is an important feature for describing the microstructure. Usually, texture is represented by pole figures, inverse pole figures (IPF) or orientation distribution functions (ODF). A more detailed description of how texture is measured and represented is given in Chapter 3.5. Some texture components are typical in aluminium alloys, and they are given in Table 2.1.

2.5.1 Deformation textures

The orientation changes during deformation occurs along the most favourable oriented slip or twinning systems. This means that they are not random, and the material acquires a preferred orientation (texture). Subsequent annealing will lead to nucleation of recrystallized grains in regions of particular orientation, and its growth ability is

Table 2.1: Overview of the typical aluminium alloy texture components, both for deformation and recrystallization textures [3].

Components (symbol)	{hkl}	<uvw>	ϕ_1	Φ	ϕ_2
copper (C)	112	111	90	35	45
S	123	634	59	37	63
Goss (G)	011	100	0	45	90
brass (B)	011	211	35	45	90
Dillamore (D)	4,4,11	11,11,8	90	27	45
cube	001	100	0	0	0
P	011	122	70	45	0
Q	013	231	58	18	0
R	124	211	57	29	63

also affected by the orientaion of the adjacent regions. This leads to characteristic recrystallization textures which develops from deformation textures.

In aluminium, which has a high stacking fault energy, cross slip is the basic deformation mechanism. It is the accommodation of the new grains to its surroundings (geometrical constraints) which causes change in orientation. A good illustration of the texture is provided by the ODF in Figure 2.8a, which shows the texture of cold rolled aluminium. One can observe that the texture is represented by a "tube" of orientations which runs from brass through S to cube, called the β-fibre. Another fibre can also be seen from Goss to brass, called the α-fibre. These tubes are schematically presented in Figure 2.8b.

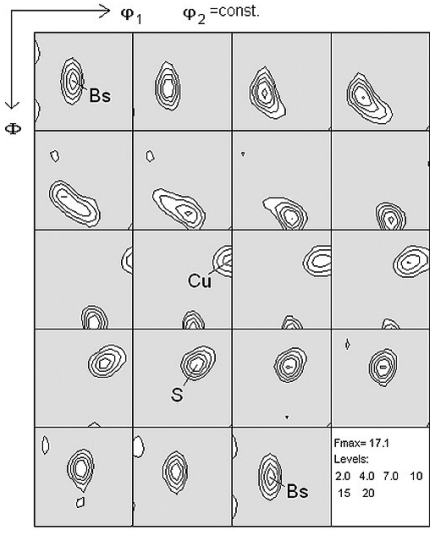

(a) ODF of cold rolled aluminium. [24]

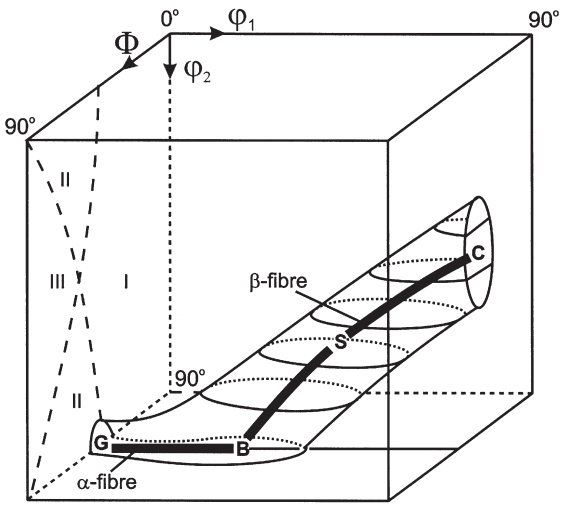

(b) Illustration offcc rolling texture in the Euler space. [25]

Figure 2.8: Schematic representations of deformation texture in cold rolled aluminium alloys.

2.5.2 Recrystallization textures

The recrystallization textures are important since they are responsible for anisotropy in the fully annealed material, which often is the starting condition for subsequent forming operations. The formation of recrystallization textures is, among other events, related to the nucleation mechanism, the boundary energy and mobility of grains in different orientations. Amount of strain and initial texture, i.e. the texture before deformation, may also be of great significance.

There are two theories on the nucleation and growth of recrystallization and how the recrystallization texture develops. The first is known as oriented nucleation, where it is assumed that the nuclei possess preferred orientations and their growth will determine the final texture. The orientations of the recrystallized microstructure must exist in the deformed state, since the formation of new orientations by recrystallization twinnning does not play an important role for aluminium. The deformed state and the recovery behaviour are therefore important for the final recrystallization texture. The other theory, called oriented growth, assumes that many nucleus orientations are formed and those with the best growth conditions with respect to the surrounding deformed matrix will determine the final texture. In particular, grains with a 40°<111> orientaion relationship to the neighbouring grains are found to have the highest growth rate in aluminium, and are therefore supposed to play an important role recrystallization textures [26]. Today it is generally accepted that recrystallization textures in aluminium results from a combination of both these mechanisms, although special circumstances may favour one or the other.

During recovery, the substructure may coarsen and little change in texture occurs. Under certain circumstances, when the high angle grain boundary movement are pinned by particles, the recovery alone can reduce the dislocation density to the level of the fully recrystallized material. In this case, the subgrain growth may eventually lead to the formation of high angle grain boundaries which look like a classic recrystallized microstructure, but the texture changes are only minor [27]. This mechanism are often referred to as continuous recrystallization, while the classical mechanism with nucleation and growth is commonly called discontinuous recrystallization.

In the case of discountinuous recrystallization, where the new undeformed grains nucleate, major texture changes may occur. The different nucleation sites often result in different textures. In the case of PSN, a weak texture with some preference to the P orientation and a rotations of the cube by 20-25° about the normal direction are observed [28]. The nucleation at cube bands and the subsequent rapid growth of cube oriented grains will obviously lead to a stronger cube texture in the final recrystallized state. Due to its favourable growth condition, several of the other deformation texture components may be compromised [29, 30]. The cube components is frequently accompanied by the R orientation, which presumably comes from nucleation at high angle grain boundaries. Subgrains on one side of the boundary starts to grow into the deformed matrix, and leads to similar orientations as those in the deformed material [31]. Subsequently the R orientaion will grow at the expense of other orientaions, since they are very different from the cube and other fast growing orientations.

2.5.3 Texture effects in grain growth

Note that recrystallization textures does not stop to develop when recrystallization is complete. Although grain growth is generally not associated with large texture changes, often only a sharpening, the texture after grain growth may still be different from the texture after primary recrystallization. The nature of the texture changes taking place during grain growth is complicated and relatively unexplored.

3 Experimental techniques

In this chapter, the theory behind the experimental techniques as well as the procedures and setup are explained. First, the materials were selected and processed related to the steps described in Chapter 2.1. The microstructure were characterized during and after processing by different methods, which is also described in this chapter.

3.1 Material selection

The work in this report is focussed on four AA1xxx alloys, called A1, A2, B1 and B2. The chemical composition of these alloys is given in Table 3.1.

Table 3.1: Chemical composition of the two alloys.

Alloy	Fe [wt%]	Si [wt%]	Al
A1	0.15	0.05	Balance
A2	0.15	0.15	Balance
B1	0.5	0.05	Balance
B2	0.5	0.15	Balance

The alloys are produced by Hydro Aluminium in Sunndalsøra as model alloys, intended for experiments and characterization. By selecting four different alloys with small but significant variations in alloying elements, the effect of difference in solute level and particle structure (i.e. constitutent particles and dispersoids) on softening behaviour can be studied.

3.2 Processing

3.2.1 Homogenization

The alloys were received as cylindrical DC-casted ingots with a diameter of 228 mm. From this, four 30×80×200 mm rolling slabs were cut out at the half radius locations of each ingot, schematically shown in Figure 3.1.

The alloys were homogenized at 600 °C followed by slow cooling. This was done to get the alloying elements out of solid solution into precipitates. By having most of the Fe and Si in stable particles before annealing, the concurrent precipitaion is most likely avoided.

The homogenization was done in an Heraeus air circulation furnace and the temperature was measured and logged with a Fluke 54II thermometer and a type K thermocouple. The time-temperature procedure was as follows: (i) Heating with 50 K/h from room temperature to 600 °C and held in 24 hours. (ii) Cooled with 20 K/h to 550 °C and held for 16 hours. (iii) Cooled with 20 K/h to 500 °C and held for 23 hours. (iv) Cooled with 20 K/h to 450 °C and held for 34 hours. (v) Quenched in water to room temperature. The temperature programme is schematically given in Figure 3.2, and all

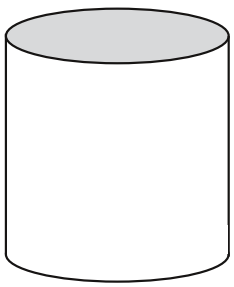

(a) The DC-casted ingot as received.

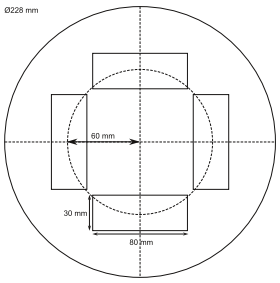

(b) The cutting scheme, as seen from top of ingot.

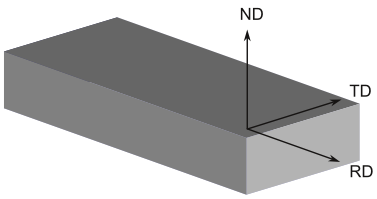

(c) The rolling slab with directions.

Figure 3.1: Illustration of where the rolling slabs were cut out from. Four slabs were cut out from each casting ingot. The normal directon (ND), transverse direction (TD) and rolling direction is denoted in Figure 3.1c.

four alloys underwent the same homogenization procedure. The measured temperature data is schematically given in Figure B.1 in Appendix B.

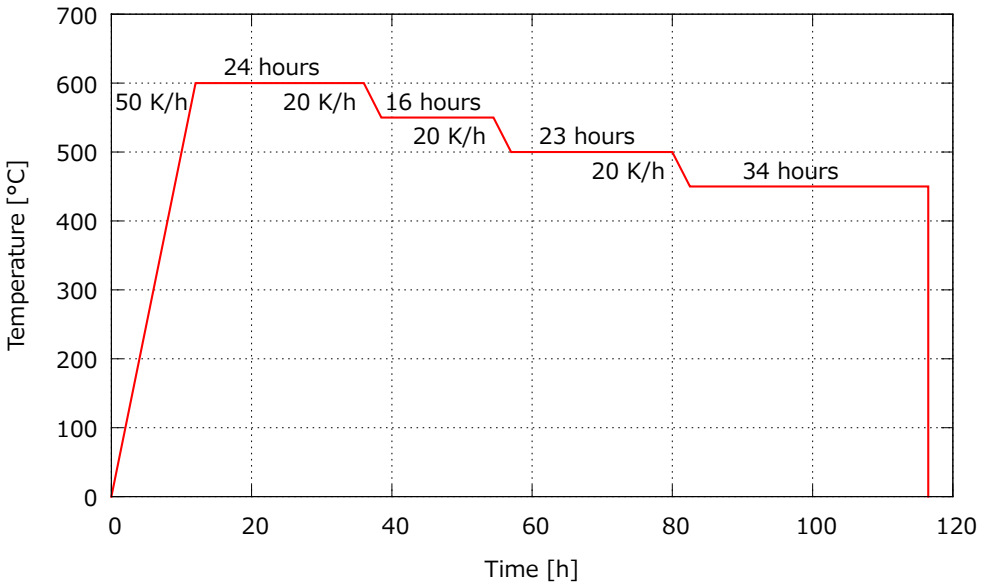

Figure 3.2: Time-temperature programme in the homogenization of the alloys. The plates were heated with 50 K/h to 600 °C and held there for 24 hours, before they were cooled gradually to 450 °C and then quenched to room temperature.

3.2.2 Cold deformation

The homogenized slabs were cold rolled at the laboratory with heavily lubricated rolls. This was done to simulate the industrial process and get the same microstructure and texture. Reduction per pass was approximately 1 mm, and the slabs were given some time to air cool between each pass. In order to preserve most of the cube-oriented grains,

the slabs were cold rolled to ϵ=2.6 [32, 33, 34]. This means that they were deformed from 30 mm to 2.2 mm thickness, which is a 92.7 % reduction.

3.2.3 Procedure for reducing the initial grain size of alloy A1

Due to a large grain size found in alloy A1, the softning kinetics of this alloy was charactarized after the initial grain size was reduced. The procedure to reduce the grain size was as follows: (i) The homogenized material was cold rolled to 15 mm, i.e. a 50 % reduction in thickness (ii) The cold rolled material was annealed to obtain complete recrystallization at 350 °C for 10^2 seconds. The microstructure was characterized in EBSD. (iii) The recrystallized material was cold rolled to at thickness of 1.1 mm, i.e. the same strain as before (ϵ=2.6) (iv) Isothermal annealing at 300 °C and characterized with hardness measurements after 5, 10, 10^2 and 10^3 seconds.

3.3 Isothermal annealing experiments

The cold rolled sheets were cut into approximately 10×10 mm specimens and isothermally annealed in salt baths or oil baths. The oil baths were used for temperatures up to 275 °C, since the salt freezes below 300 °C. For the annealing experiments with short holding times, i.e. 5 and 10 seconds, the specimens were manually stirred in order to reduce heating time. The effect of stirring is of greater significance for thick samples and at the shortest annealing times, see figure, see Figure 3.3 [8]. The temperature was measured with an Amprobe TM45A thermometer and a type K thermocouple. After annealing, the samples were quenched in water immidiately.

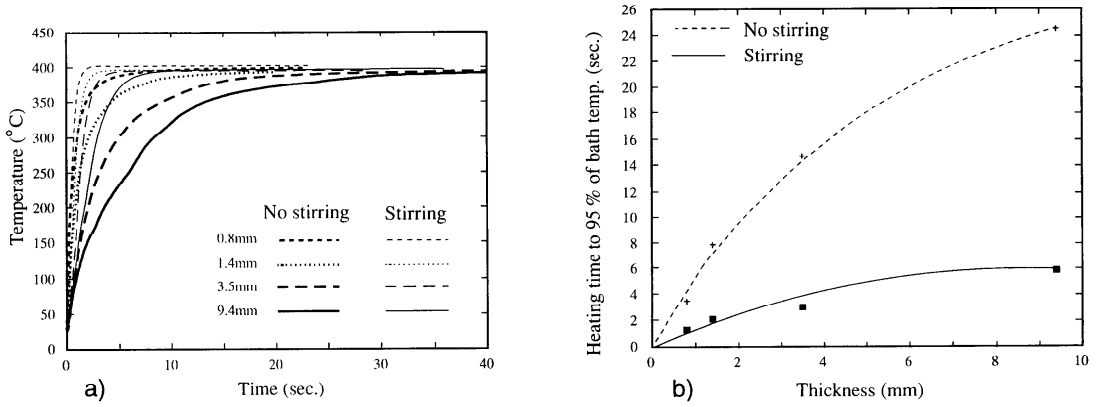

(a) Heating rate to 400 °C for different sample thicknesses.

(b) The time to 95% of salt bath temperature against thickness.

Figure 3.3: The effect of stirring during annealing in salt baths [8].

3.3.1 Hardness test

Hardness was measured to follow the mechanical properties during annealing. The Vickers hardness test measures resistance to penetration of a diamond pyramid. The hardness

numbers are effective for qualitative comparison of the softening evolvement. Vickers hardness was measured with a Matsuzawa DVK-1S instrument with a load of 1 kg, a loading speed of 100 μm/s and 15 seconds holding time. The samples where grinded on a 1200 mesh SiC paper. The average of five indentations on the RD-TD plane is used in the results.

3.3.2 Electrical conductivity measurements

The presence of alloying elements in solid solution will decrease the electrical conductivity of aluminium. This is due to their distortion of the lattice. If the alloying elements appears in incoherent particles, the effect on electrcal conductivity is much less. By measuring the electrical conductivity before and during the annealing, it is possible to get information about content in solid solotion and concurrent precipitaion. By using a modified version of the Matthiessens rule, the solid solution content of the different alloying elements and the electrical conductivity can be related [35]:

$$\frac{1}{\kappa} = 0.0267 + 0.036Mn + 0.032Fe + 0.0068Si, \tag{3.1}$$

where κ is the electrical conductivity [m/Ωmm^2] and Mn, Fe and Si are solid solution content [wt%] for these elements.

The electrical conductivity was measured with a Foerster Sigmatest 2.069 portable eddy current test instrument. The probe was mounted on the same sample surface as on which the hardness was measured, i.e. on the RD-TD plane. The conductivity measurements were done after the hardness was measured. A measuring frequency of 120 kHz was used. According to the operating instructions from Foerster, accurate values can be guaranteed on samples thinner than 1 mm when using 120 kHz measuring frequency [36]. However, these results are only an estimate, and it is impossible to seperate the contribution from the various elements. The average of five measurements are used in the results.

3.4 Microstructural and texture characterization

3.4.1 Optical light microscpy

Optical microscopy is in this work used for imaging and grain size measurements. The Leica MEF4M was used with polarized light and a sub-parallel λ-plate. The sample preperation for optical light microscopy was as follows: (i) Embedding in ClaroCit mounting resin. (ii) Grinding on SiC paper with the mesh sizes 320, 500, 800, 1200 and 2400. (iii) Diamond polishing with grain sizes 6 μm, 3 μm and 1 μm. (iv) Electro polishing for 10 seconds at 20 V in electrolyte containing 20% $HClO_4$ and 10% H_2O. The temperature of the electrolyte was −35 °C using the Julabo refrigiated circulator. (v) Anodized for 100 seconds at 20 V in 5% HBF_4 aqueous solution.

3.4.2 Scanning Electron Microscopy imaging

Scanning electron microscopy (SEM) has in this work been used for both imaging of particle structure and for the EBSD-scans, which is described Chapter 3.4.3. For imaging of particles, the backscatter detector in the Hitachi SU-6600 FESEM was used to obtain Z-contrast. An acceleration voltage of 5 kV, probe current "Large" and the apertures in the recommended optimum positions were used. The sample preperation for SEM imaging was as follows: (i) Embedding in ClaroCit mounting resin. (ii) Grinding on SiC paper with the mesh sizes 320, 500, 800, 1200 and 2400. (iii) Diamond polishing with grain sizes 6 µm, 3 µm and 1 µm.

Analysis of SEM images The SEM images of the particles was analysed in the ImageJ software. The images was converted to 8-bit grayscale and then to binary images. The fraction of the white area and the mean size was then measured by the software.

3.4.3 Electron backscatter diffraction

The electron backscatter diffraction (EBSD) method is used to determine the crystallographic orientations. Experimentally, EBSD is carried out by using a SEM together with a phosphor screen and a CCD camera, called the EBSD detector. The setup inside the vacuum chamber is shown in Figure 3.4b. The incident electron beam hits a tilted sample, and some of the electrons will be elastically scattered, and a fraction of these will be diffracted according to the well-known Bragg's law:

$$2d \sin\theta = n\lambda, \tag{3.2}$$

where d is the interplanar distance, θ is the inclination angle and λ is the wavelength of the incoming beam. The interplanar distance is given by:

$$d = \frac{a_0}{\sqrt{h^2 + k^2 + l^2}}, \tag{3.3}$$

where a_0 is the lattice parameter and h, k and l are the Miller indices. When the conditions for Bragg's law is fulfilled, the scattered electrons gives constructive interference and results in a Kikuchi pattern (an example is shown in Figure 3.4b), which represent the atomic planes $\{hkl\}$ of the crystal at that position. The patterns are captured by the EBSD detector, and before further processing, the background is subtracted to get better contrast. The patterns are indexed by relating the bands to points with a process called Hough transformation.

The EBSD technique is in this work used for grain size, local texture and recrystallization measurements, as well information about misorientation angles. The Hitachi SU-6600 field emission SEM (FESEM) equipped with a NORDIF UF1000 EBSD detector was used for these experiments. The sample preperation for EBSD was as follows: (i) Embedding in ClaroCit mounting resin. (ii) Grinding on SiC paper with the mesh sizes 320, 500, 800, 1200 and 2400. (iii) Diamond polishing with grain sizes 6 µm, 3 µm and 1 µm. (iv) Electropolishing for approximately 10 seconds at 20 V in electrolyte containing 20% $HClO_4$ and 10% H_2O using the LectroPol-5 apparatus. The temperature of the electrolyte was -35 °C using the Julabo refrigiated circulator.

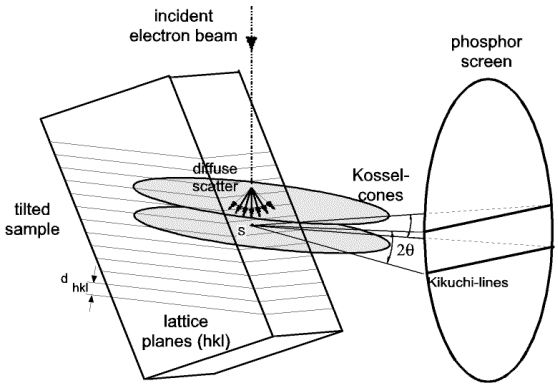

(a) Schematic illustration of the EBSD setup.

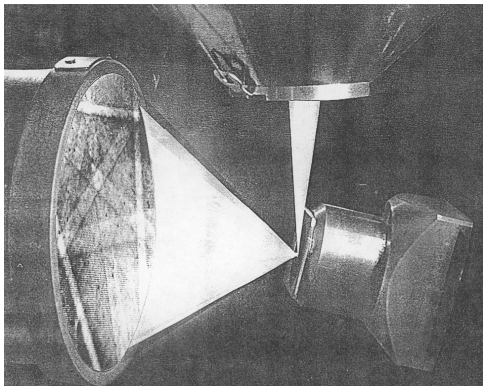

(b) Illustration from inside the SEM.

Figure 3.4: Illustration of the EBSD setup. The incident electron beam hits the tilted sample and gives rise to Kikuchi lines, detected on the phosphor screen. The bands in the Kikuchi patterns are representing lattice planes, used to identify the crystallographic orientations [37].

FESEM setup The acceleration voltage of the FESEM was 20 kV and the working distance was kept between 24 and 28 mm, as the optimal is ∼26 mm. The probe current was set to "Large" and the apertures in the recommended optimum positions. The samples were tilted 70°.

Pattern collection setup To collect all the patterns, the NORDIF 1.4.0 software was used in offline mode. There are several parameters in this software to adjust to get the optimal resolution, scanning rate and exposure time. Some of these parameters may vary from sample to sample due to different grain size and degree of recrystallization. The operating parameters for the pattern collection are given in Table 3.2, both for the calibration patterns and the acquisition patterns.

Table 3.2: Typical operating parameters for pattern collection in the NORDIF UF-390 software.

Parameter	Calibration	Acquisition
Frame rate [fps]	200	500
Resolution [px]	240×240	96×96
Exposure time [µs]	4500	1000

A minimum of five calibration patterns were collected in order to calibrate for the pattern center before indexing. The collected patterns were indexed by using the TSL OIM Data Collection 6 software. During indexing, the "fit" and "confidence index" (CI) parameters gives the quality of the patterns. The fit parameter defines the average angular deviation between the calculated bands where they should appear and the detected bands. The value of CI gives the probability of correctly indexed patterns.

EBSD data analysis All analysis of the collected patterns were done by using TSL OIM Analysis 6.1 software. Some processing and clean up must be done to get the correct and good measurements. With every EBSD-map, the following procedure were performed in the software: (i) Rotated 90° around the RD axis, as the software automatically assumes that all maps are in the RD-TD-plane. (ii) Grain CI standardization. This changes the CIs of all points in a grain to the maximum CI found among all points belonging to the grain. (iii) Grain dilatation. A point that do not belong to any grains is included in the grain which have the majority of neighbouring points. (iv) Neighbour CI correlation. If a point has a CI less than a defined minimum value then the CIs of the nearest neighbours are checked to find the neighbour with the highest CI. (v) Minimum grain size and misorientation set to remove the poorly indexed points that the software takes as small grains.

The grain size in all the recrystallized samples is measured in the EBSD software with the linear intercept method, with minimum misorientation of 5°.

3.5 Global texture measurements

Texture is usually measured by X-ray diffraction and presented in pole figures. A pole figure is a stereographic projection which shows the distribution of a crystallographic direction in the sample. It must contain a reference direction that relates to the sample itself. For example, the rolling direction must be denoted in the pole figure. To represent the cube faces in the stereographic projection, a unit cube is located in the origin of the reference coordiante system, surrounded by a unit sphere. The point of intersection of the normal vector of each cube face, i.e. the <100>-planes, with the unit sphere is determined. A line from these points, which lies in the northern hemisphere, to the south pole of the unit sphere, intersect the equatorial plane and are called poles of the respective cube faces. The <111> pole figure, which is most widely used for alumium, is obtained by using the normal vectors of the <111>-planes instead of the <100>-planes. The typical deformation and recrystallization components in aluminium is given in Figure 3.5.

For polycrystalline materials, the set of poles plotted for each individual grain to produces the pole figure. For more than one orientation, the pole figure is limited since one orientation has several poles, and there is no way of obtaining a complete orientiation of individual grains. The orientation distribution function (ODF) makes use of the unique rotation of the grains in terms of Euler angles, and provides a better description of all the orientations of all the descrete volumes in the aggregate.

The ODFs use two reference systems, one sample and one crystal reference system. For the sample reference system it is most convenient to choose the directions that coincide with the rolling direction (RD), the transverse direction (TD) and the normal direction (ND). The crystal reference system has x-, y- and z-axes fit with the cubic axes [100], [010] and [001]. The Bunge notation is a common way to define the rotation of the crystal system compared to the sample system [38]. Here, the Euler angles $g = \{\phi_1, \Phi, \phi_2\}$ defines the rotation between the two coordinate systems. The crystal system, which is the variable one, is put parallel to the sample system and rotated about the z-axis, ϕ_1,

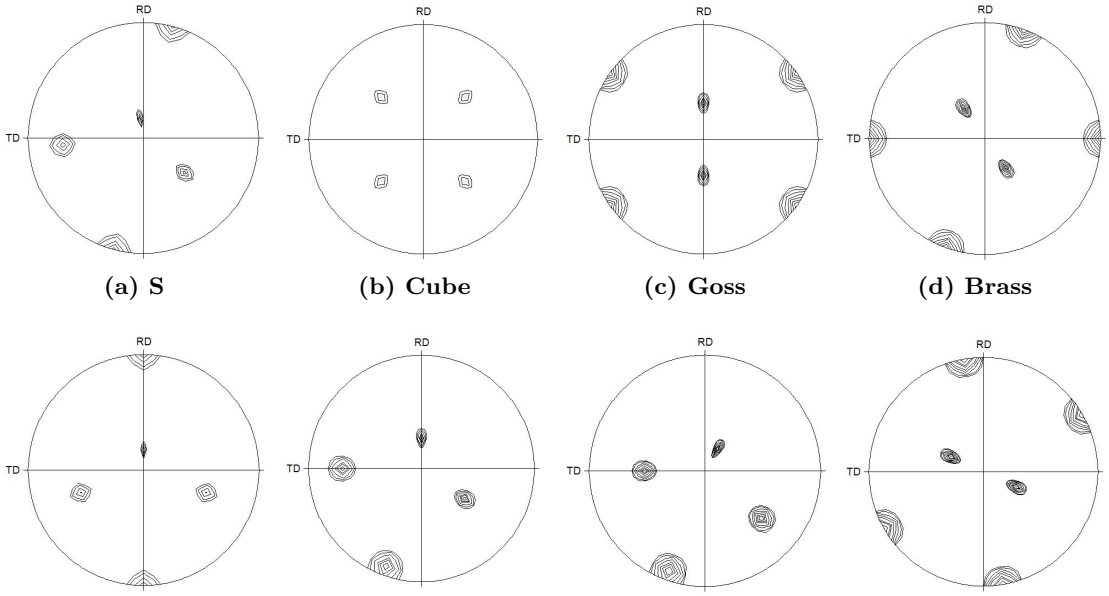

(a) S (b) Cube (c) Goss (d) Brass

(e) Copper (f) R (g) BR (h) P

Figure 3.5: The <111> pole figures for the most typical aluminium texture components.

the x-axis, Φ, and about the z-axis again, ϕ_2. An example of this is shown in Figure 3.6a. To represent the three angles in two dimensions, ϕ_2 is divided into 5° intervals.

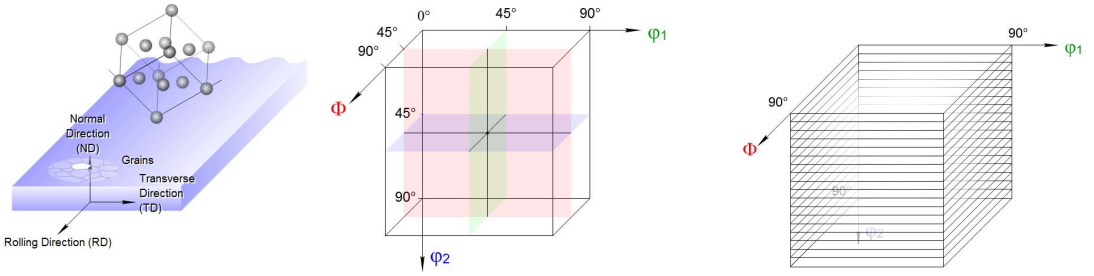

(a) Cold rolled sheet with a grain oriented 45° around all three sample reference system axes, and represented in the 3D graph to the right.

(b) The 3D graph divided into ϕ_2=5° intervals, which makes up the ODF.

Figure 3.6: Representation of texture with Euler angles, which is the basis of the ODF [39].

Each grain represents an orientation g. The definition of the texture is given by a ODF, which gives the volume fraction of the orientation g:

$$f(g) = f(\phi_1, \Phi, \phi_2) = \frac{dV(g)/V}{dg}, \tag{3.4}$$

where V is the total sample volume and $dV(g)$ is the totality of all volume elemts of the sample which posess the orientaion g within the element of orientaion dg. This function is calculated from measured pole figures.

The conventional way to measure the global texture in a samle is to use X-ray diffraction,

and is used in this work. The sample is mounted in a two-circle goniometer which simultaneously can permit four different movements. The beams which are restricted by a series of slits are set at the appropriate Bragg angles for diffraction from the required plane. A pole figure for a given plane is measured by selecting the angle which gives diffraction according to Bragg's law, and keeping it constant throughout the measurement. At least four pole figures are needed, and by rotating and tilting the sample, the distribution of the plane normals of the desired $\{hkl\}$ plane is recorded. In this work, the (111), (200), (220) and (311) pole figures was used.

The Siemens D5000 diffractometer equipped with a Hüber Eulerian cradle was used for these experiments, together with the Bruker DIFFRAC plus software. The X-ray diffractometer samples were prepared as follows: (i) Samples of 14×22 mm in the RD-TD-plane were cut out from the cold rolled sheets. (ii) Grinding from initial 2.2 mm thickness to approxemately 1.9 mm thckness in order to avoid the surface deformation texture. (iii) Grinding on SiC paper with the mesh sizes 320, 500, 800, 1200 and 2400. (iv) Etching for 5 minutes in 20 % NaOH aqueous solution.

4 Results

The main objective of this work has been to investigate the softening behaviour of four commercially pure aluminium modelling alloys, named A1, A2, B1 and B2. The experimental results of the four alloys will be presented in Chapter 4.1, side by side, chronologically from start of the processing to the final annealing.

4.1 Characterization

4.1.1 Initial material

A brief characterization of the as-cast microstructure were carried out to check the condition of the received material. The grain sizes and electrical conductivities are given in Table 4.1. The grain size distributions are given in Appendix A. For alloy A1, the grain size distribution looks slightly more inhomogenous than the other alloys, with the dominating grain size larger than 100 µm. The grain size in alloy A1 is larger than the three others, approximately 50 %. Only minor differences in alloy A2, B1 and B2 are observed. Alloy A1 also has more elongated grains than the three other alloys, see Figure 4.1. The grain sizes are measured from EBSD-maps from only one sample of the rolling billet, and these grain sizes should therefore only be taken as approximate values.

Table 4.1: Grain size, area fraction of particles and electrical conductivity in the as-cast alloys. Grain sizes are measured from EBSD-maps.

Alloy	Grain size [µm]	Electrical conductivity [m/Ωmm^2]
A1	139.7	34.76
A2	83.4	34.89
B1	81.4	33.37
B2	90.3	32.84

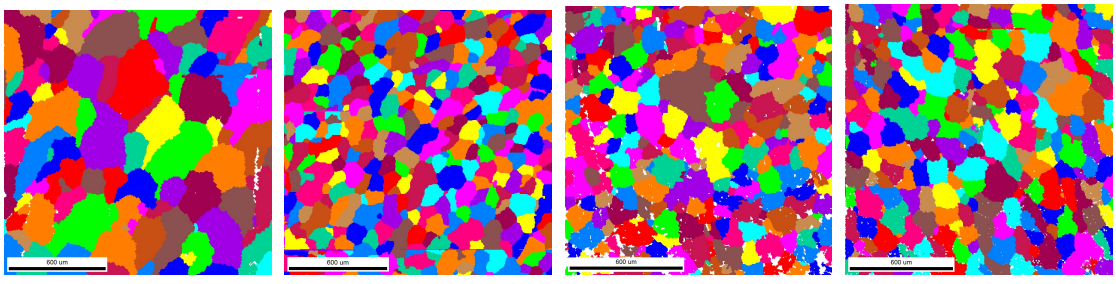

(a) Alloy A1 (b) Alloy A2 (c) Alloy B1 (d) Alloy B2

Figure 4.1: Unique grain colour maps from EBSD at 50X magnification of the as-cast state, as seen on the RD-ND-plane on the rolling slab. The white areas are unindexed points.

4.1.2 Homogenized material

As the initial material, the microstructure of the homogenized material was characterized with respect to grain size and electrical conductivity, given in Table 4.2. The grain size distributions are given in Appendix A. The grain size of Alloy A2 were to large and inhomogenous to be measured accurately from the EBSD-maps. The electrical conductivity values are used to calculate the amount of Fe in solid solution from Equation 3.1, with all Si assumed to be in solid solution.

Table 4.2: Grain size, area fraction of particles and electrical conductivity in the homogenized alloys. Grain sizes are measured from EBSD-maps.

Alloy	Grain size [μm]	Electrical conductivity [m/Ωmm^2]	Fe in ss [wt%]
A1	128.8	35.52	0.03
A2	-	35.64	0.01
B1	84.7	35.01	0.05
B2	72.1	34.64	0.04

For alloy A1 and B2, the grain size is lower that of the as-cast material. The grain sizes are measured in the same plane, but the position of the billet is not the same. For alloy B2 and A1, the grains sizes are a little higher than in the as-cast material.

SEM images of the particle structure are presented in Figure 4.2. The particles which are visible in these images are the large, undeformable particles which may act as nucleation sites for PSN. An estimation of the area fraction and particle size was measured from binarized versions of images as in Figure 4.2. These results are given in Table 4.3. As expected, more particles are seen in alloy B1 and B2 than alloy A1 and A2, as the content of iron are higher in these.

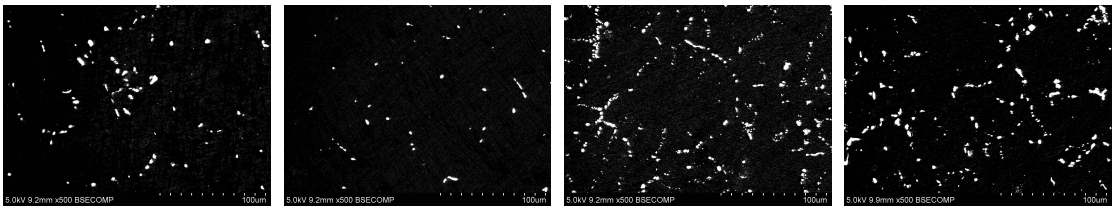

(a) Alloy A1 **(b) Alloy A2** **(c) Alloy B1** **(d) Alloy B2**

Figure 4.2: Particles in the homogenized material as seen in 500X SEM images taken with the backscatter detector.

Table 4.3: Area fraction and size of particles in the homogenized material.

Alloy	Area fraction	Average size [μm]
A1	0.004	2.2
A2	0.003	3.5
B1	0.012	2.2
B2	0.008	2.4

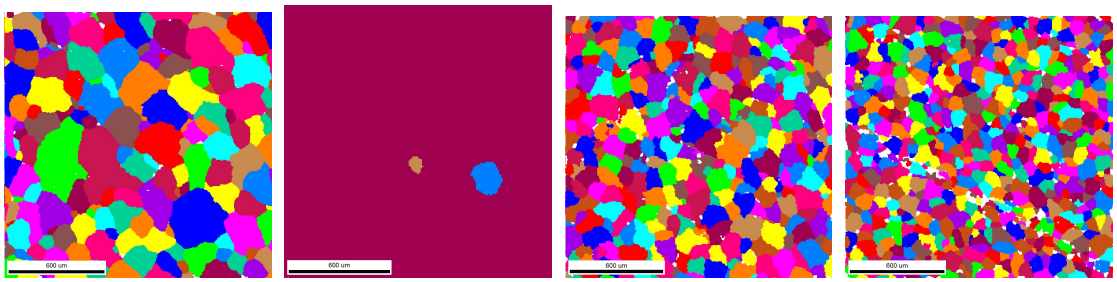

(a) Alloy A1 (b) Alloy A2 (c) Alloy B1 (d) Alloy B2

Figure 4.3: Unique grain colour maps from EBSD at 50X magnification of the homogenized state, as seen on the RD-ND plane on the rolling slab. The white areas are unindexed points.

Images of microstructure from EBSD-maps are given in Figure 4.3. Alloy A1, B1 and B2 have a relatively homogenous grain size distribution. As seen in Figure 4.3b, the microstructure of alloy A2 is not like the other alloys. The grains in this alloy is much larger, which is also observed in the optical light microscope, see Figure 4.4. The image is taken in the RD-ND plane near the edge of the rolling slab. Further discussion of this is given in Chapter 5.1.2.

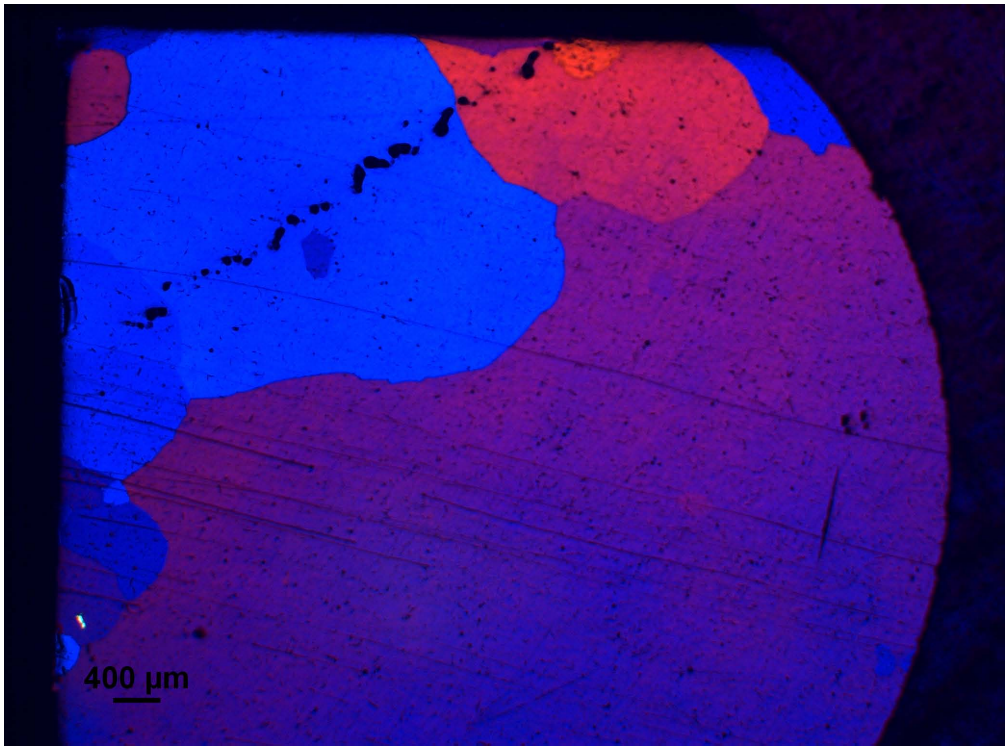

Figure 4.4: Alloy A2 in the homogenized state as seen in the optical light microscope at 2.5X magnification.

4.1.3 Cold rolled material

The homogenized alloys were cold rolled where they were reduced from 30 mm to 2.2 mm in thickness, corresponding to a true strain of 2.6. The microstructure was studied in an optical light microscope, and images are given in Figure 4.5. Alloy A1, B1 and B2 have the typical deformed microstructure with several high angle grain boundaries, as the sharp colour contrasts indicate. Alloy A2 have fewer locations with the same orientation differences. However, there are the smaller bands inside the large blue region which seems to be of different orientation.

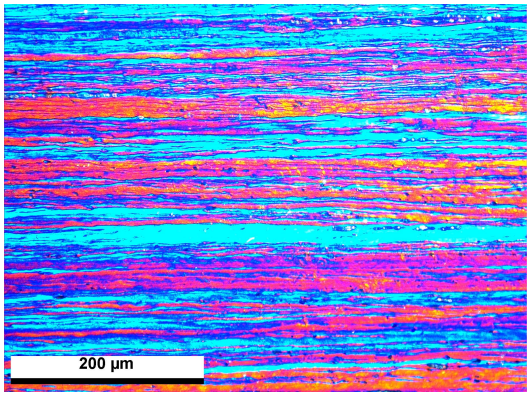

(a) Alloy A1

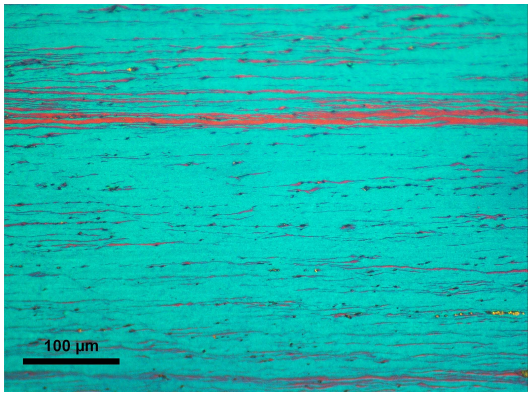

(b) Alloy A2

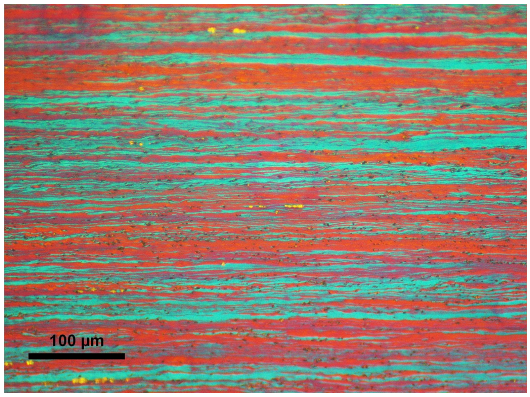

(c) Alloy B1

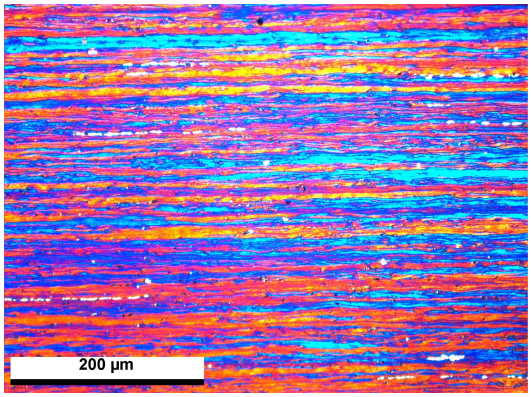

(d) Alloy B2

Figure 4.5: The deformed state in optical light microscope at 20X magnification.

Global texture Texture plots as ODFs of the deformed material are given in Figure 4.6. Comparing with Figure 2.8a, one generally see that the Goss texture component are weak in all four alloys. On the other hand, the brass, S and copper components (the β-fibre) are strong in the deformed alloys. The brass and S components are slightly stronger in alloy A1 and A2 than in alloy B1 and B2. The cube texture component seems to be missing in all four alloys. The maximum levels are considerably higher in alloy A2, as the large grain size may give insufficient statistics. In this alloy, the S peak seems to be shifted towards the R peak.

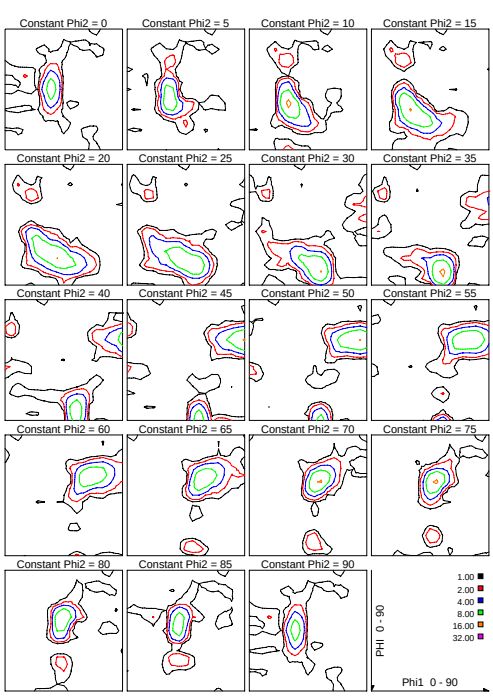

(a) Alloy A1. $f_{max} = 16.13$

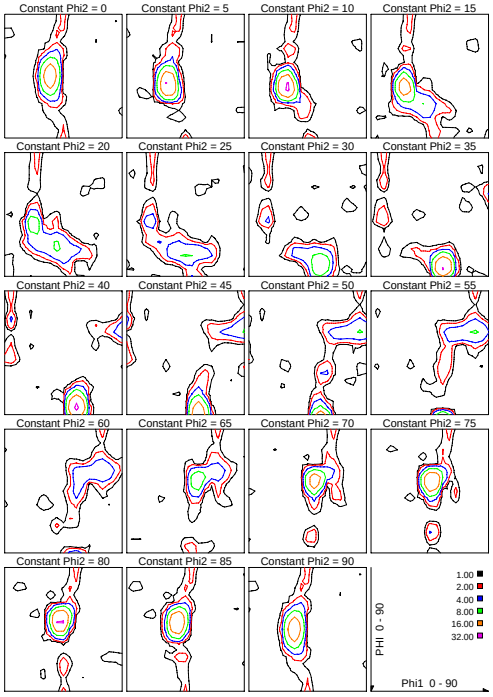

(b) Alloy A2. $f_{max} = 41.17$

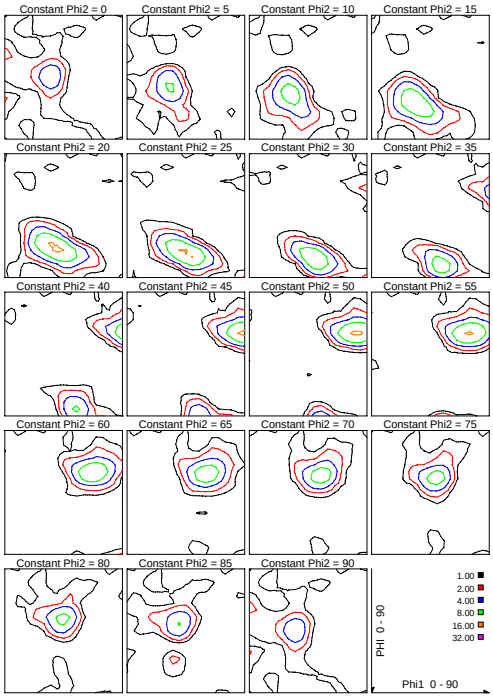

(c) Alloy B1. $f_{max} = 16.55$

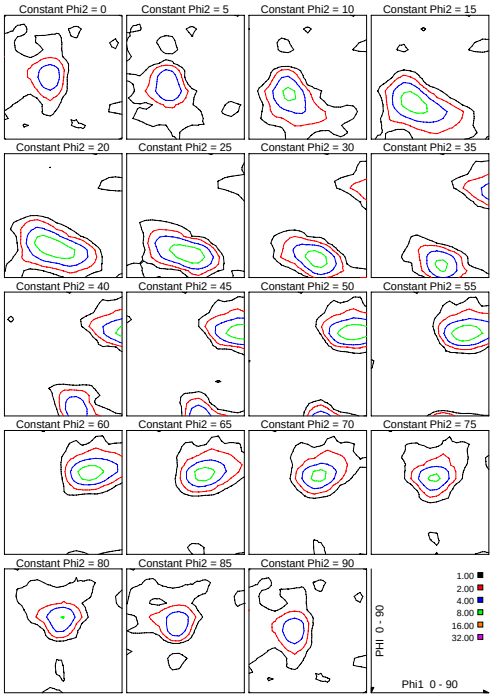

(d) Alloy B2. $f_{max} = 10.48$

Figure 4.6: ODF of the alloys in the deformed state. Note that the lines with the same colour has the same intensity for all figures. Volume fraction of the grains of certain orientations are given as f_{max}.

4.1.4 Isothermally annealed material

The isothermal annealing of the four alloys was followed with hardness and electrical conductivity measurements. These results are presented graphically in Figure 4.7-4.10 (on the next pages). The average values at 10^5 seconds annealing for the different temperatrues are given in Table 4.4.

Table 4.4: Hardness and electrical conductivity after annealing for 10^5 seconds, given as the average at the different temperatures.

Alloy	Hardness (HV)	Electrcal conductivity [m/Ωmm^2]
A1	19.9	35.8
A2	21.3	35.2
B1	22.1	35.3
B2	22.8	34.9

The curves with hardness plotted as function of annealing time, often called softening curves, shows that all four alloys stabilize at a certain value. This is the hardness value of the alloys when they are fully recrystallized, see Table 4.4. Almost no changes in this value are observed after further annealing.

The hardness values of alloy B1 and B2 sligthly decrease more rapid than alloy A1 and A2, i.e. they are somewhat faster to reach fully recrystallized state. For instance, when annealing at 350 °C, the hardness of alloy B1 and B2 reaches recrystallized hardness values after 10^2 seconds while alloy A1 and A2 are fully recrystallized after 10^3 seconds. Several of the softening curves in Figure 4.7a-4.10a do not follow a the typical behaviour explained in Chapter 2.3. These curves, the curves of alloy B2 (Figure 4.10a) in particular, are quite linear on the logarithmic time scale and do not have the classic drop at the onset of recrystallization.

Generally, the electrical conductivity increases with increasing annealing time. A little tendency towards a value that stabilize can be observed, although the value continues to increase throughout the annealing time, especially for alloy A2 and B2. While the elctrical conductivity in alloy A1 stabilize at around 35.2 m/Ωmm^2 for the four highest temperatures, the material annealed at 275 °C have a increase of 0.4 m/Ωmm^2 from 10^4 to 10^5 seconds annealing time. Alloy A2 has the largest gap in values between the material annealed at the higher temperatures and the lower temperature, of approximately 0.6 m/Ωmm^2. In this alloy, the electrical conductivity continues to increase for the low temperatures, and stabilizes or decrease slightly for the high temperatures.

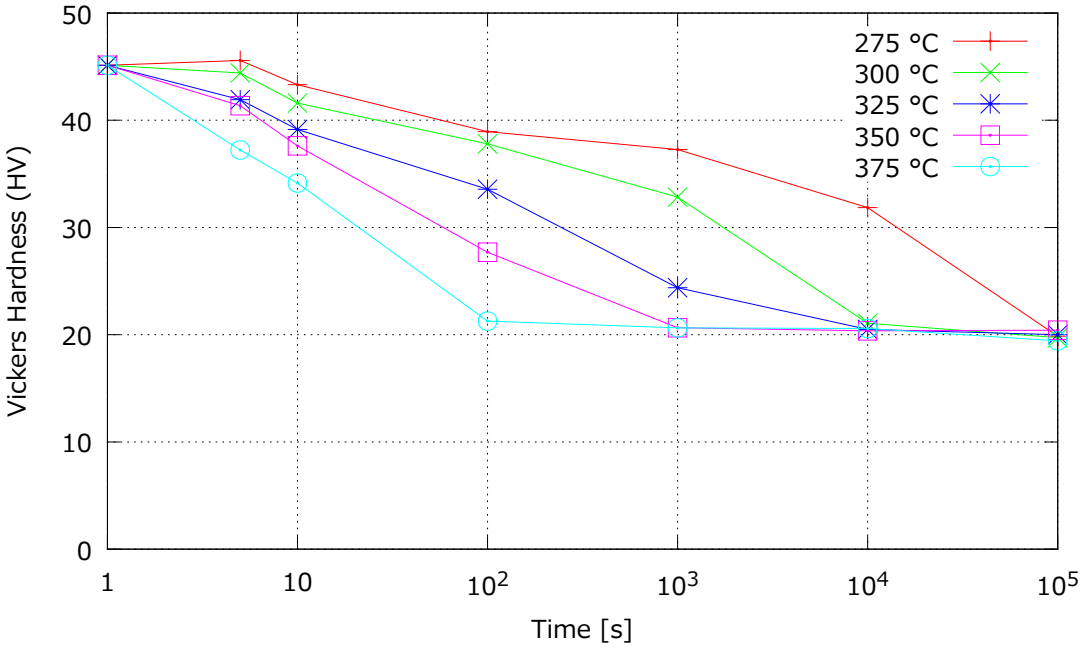

(a) Vickers hardness versus time during isothermal annealing.

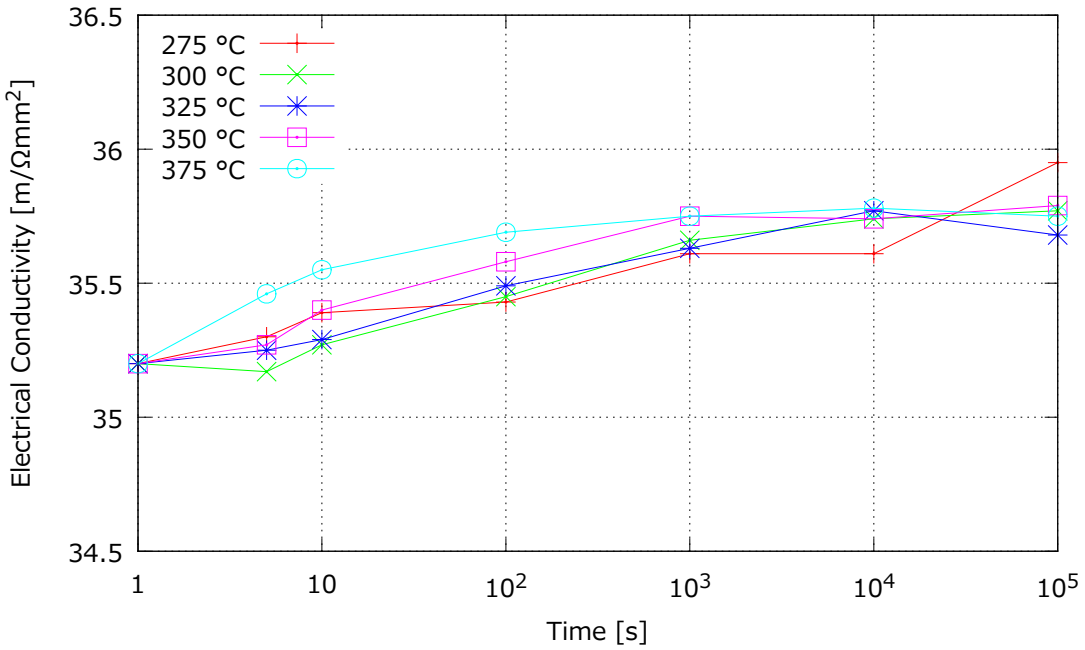

(b) Electrical conductivity versus time during isothermal annealing.

Figure 4.7: The mechanical and physical properties of alloy A1 during isothermal annealing.

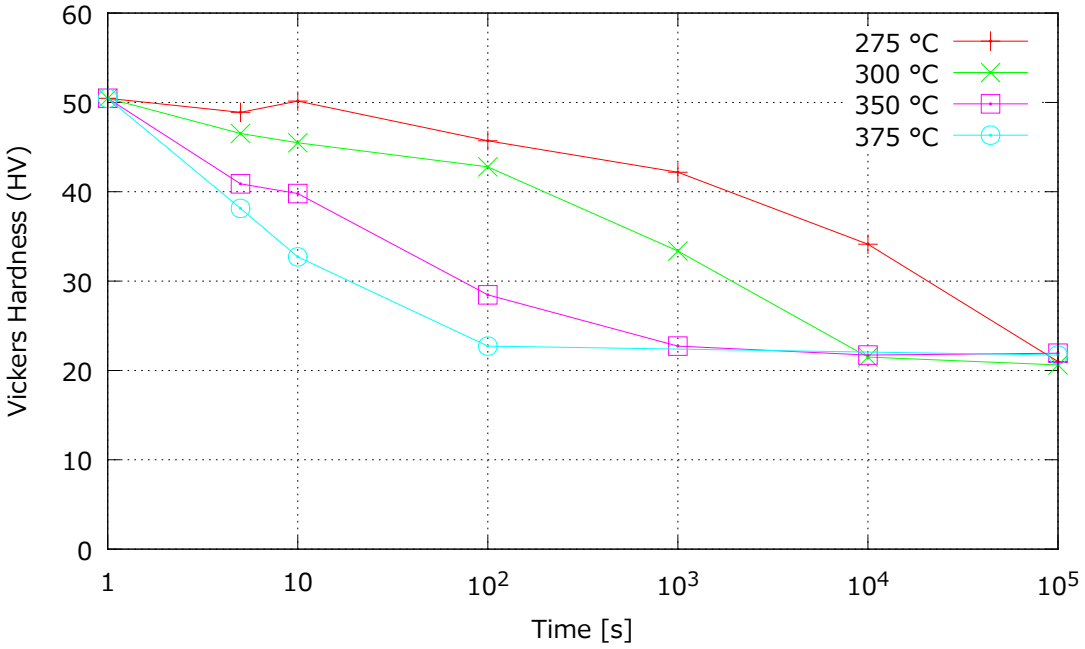

(a) Vickers hardness versus time during isothermal annealing.

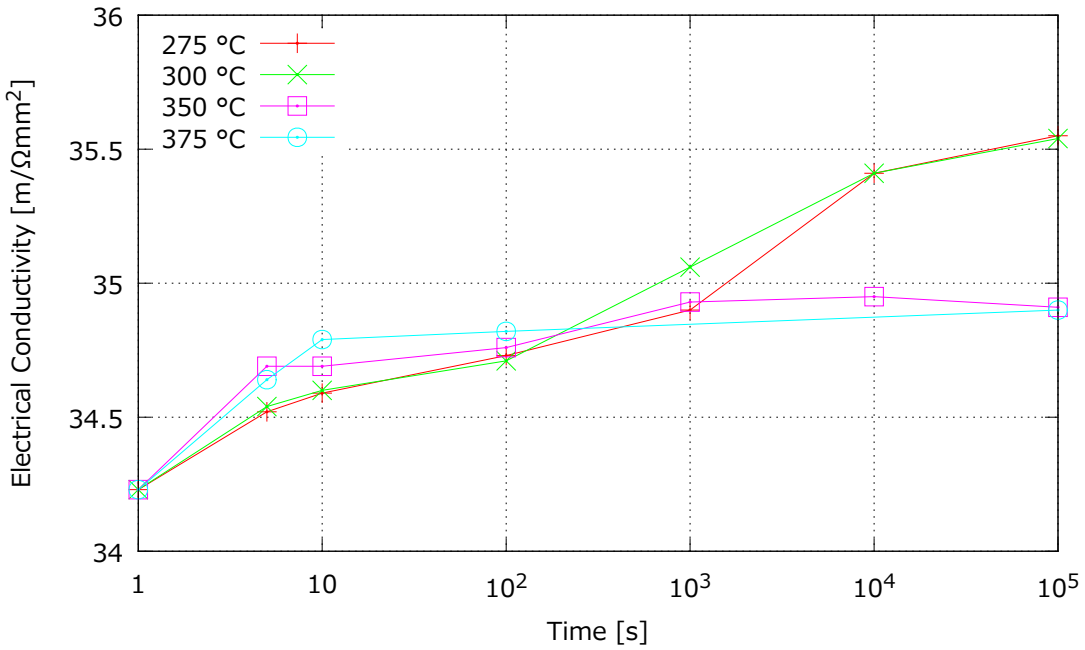

(b) Electrical conductivity versus time during isothermal annealing.

Figure 4.8: The mechanical and physical properties of alloy A2 during isothermal annealing.

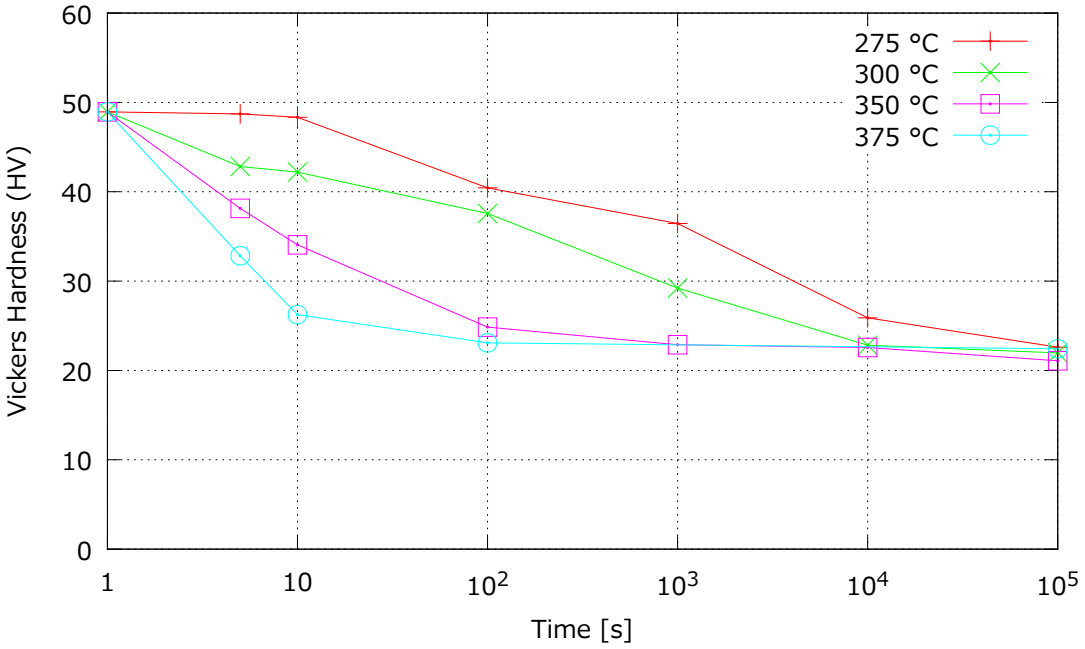

(a) Vickers hardness versus time during isothermal annealing.

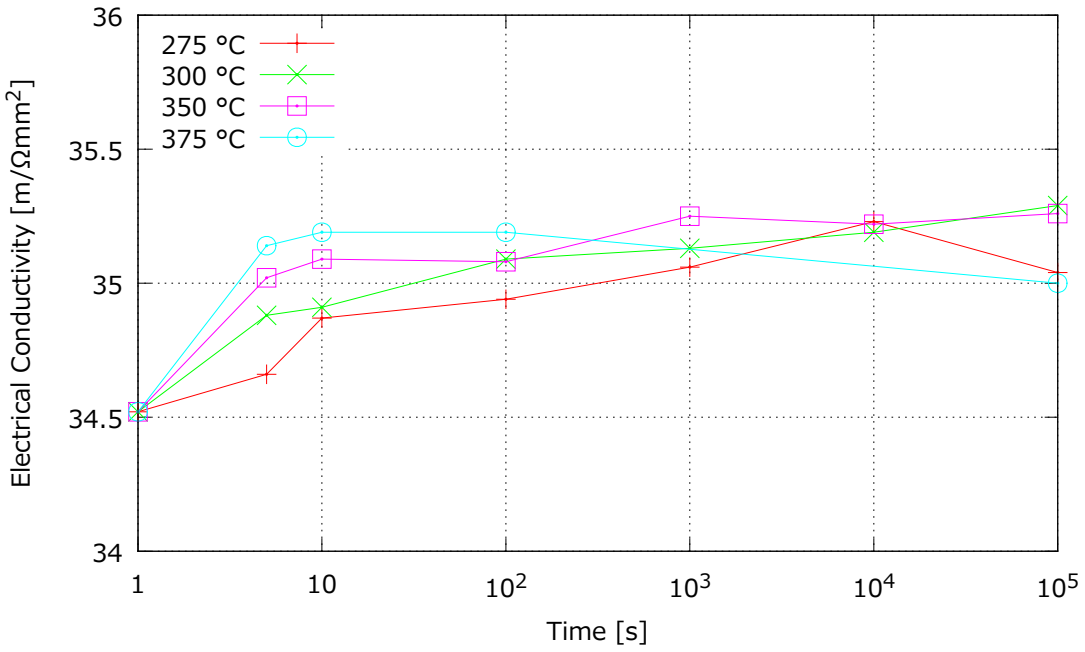

(b) Electrical conductivity versus time during isothermal annealing.

Figure 4.9: The mechanical and physical properties of alloy B1 during isothermal annealing.

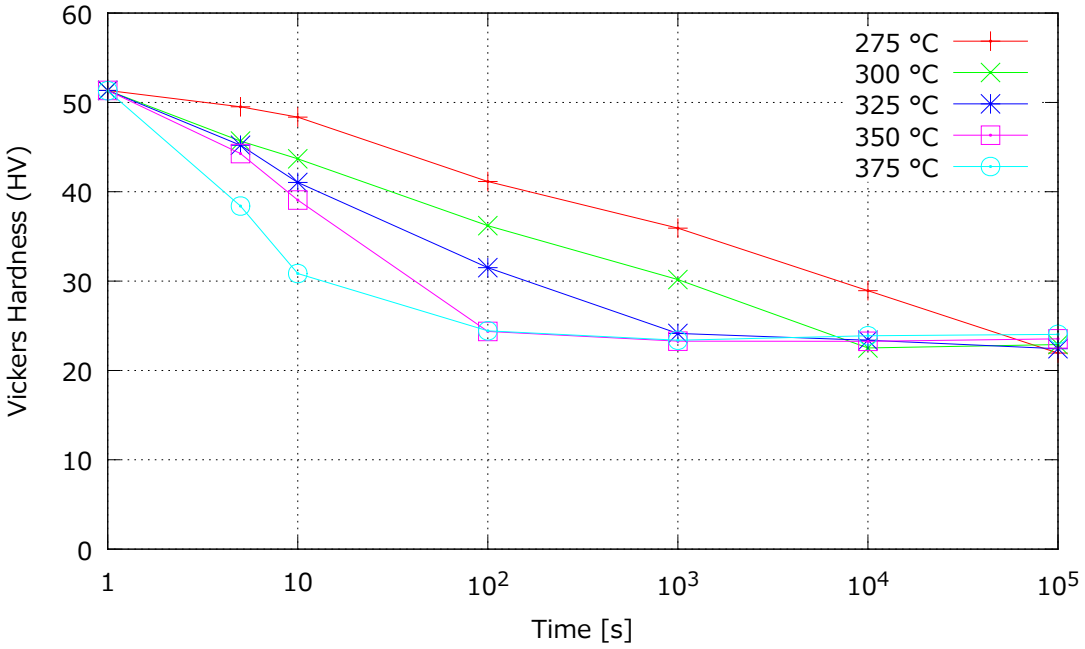

(a) Vickers hardness versus time during isothermal annealing.

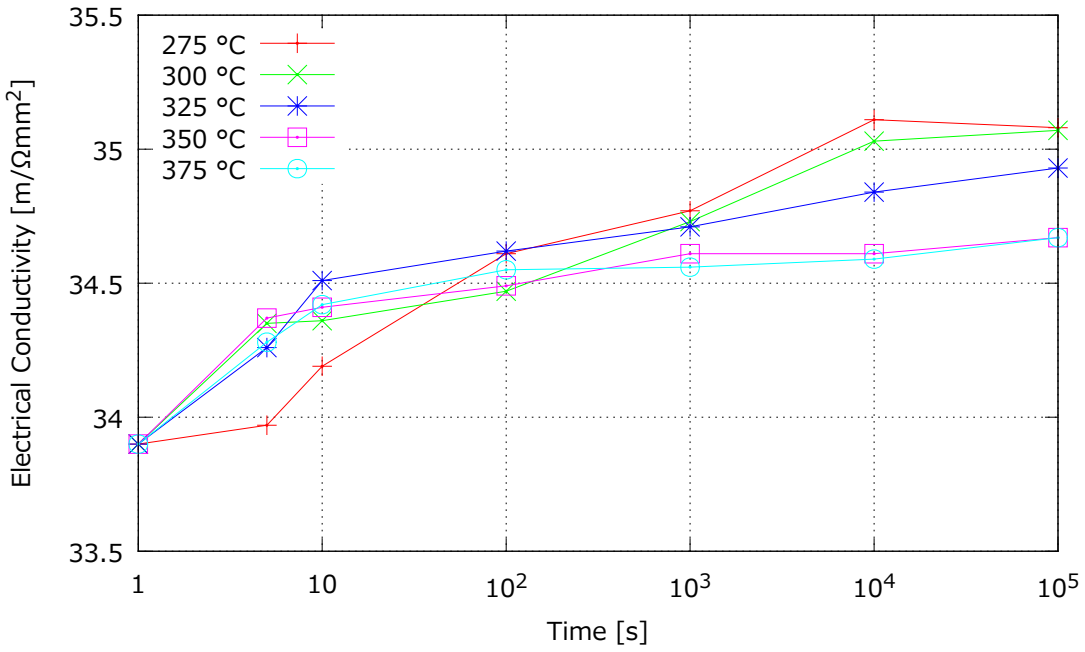

(b) Electrical conductivity versus time during isothermal annealing.

Figure 4.10: The mechanical and physical properties of alloy B2 during isothermal annealing.

The inverse pole figures from EBSD-maps for alloy A1 during annealing at 275 °C are given in Figure 4.11. At this temperature, grains seems to be nucleating after 10^2 seconds, while the largest growth of nucleated grains is happening when annealing from 10^4 to 10^5 seconds.

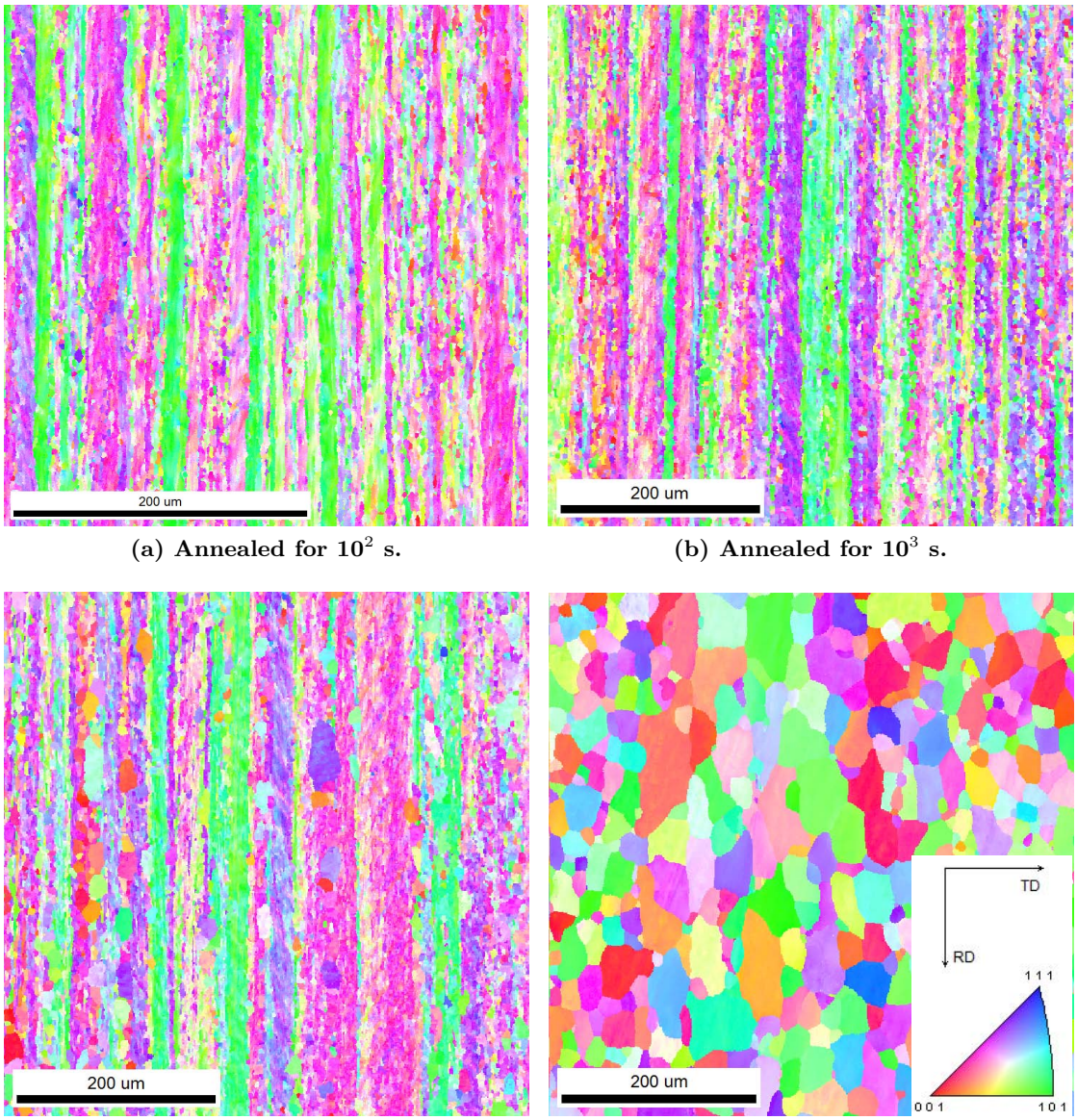

(a) Annealed for 10^2 s. **(b) Annealed for 10^3 s.**

(c) Annealed for 10^4 s. **(d) Annealed for 10^5 s.**

Figure 4.11: IPF from EBSD-maps of alloy A1 during annealing at 275 °C

The inverse pole figures from EBSD-maps for alloy B2 during annealing at 275 °C are given in Figure 4.12. Nucleation and growth of nucleated grains seems to be happening already from 10^2 seconds annealing time, gradually growing into a fully recrystallized state.

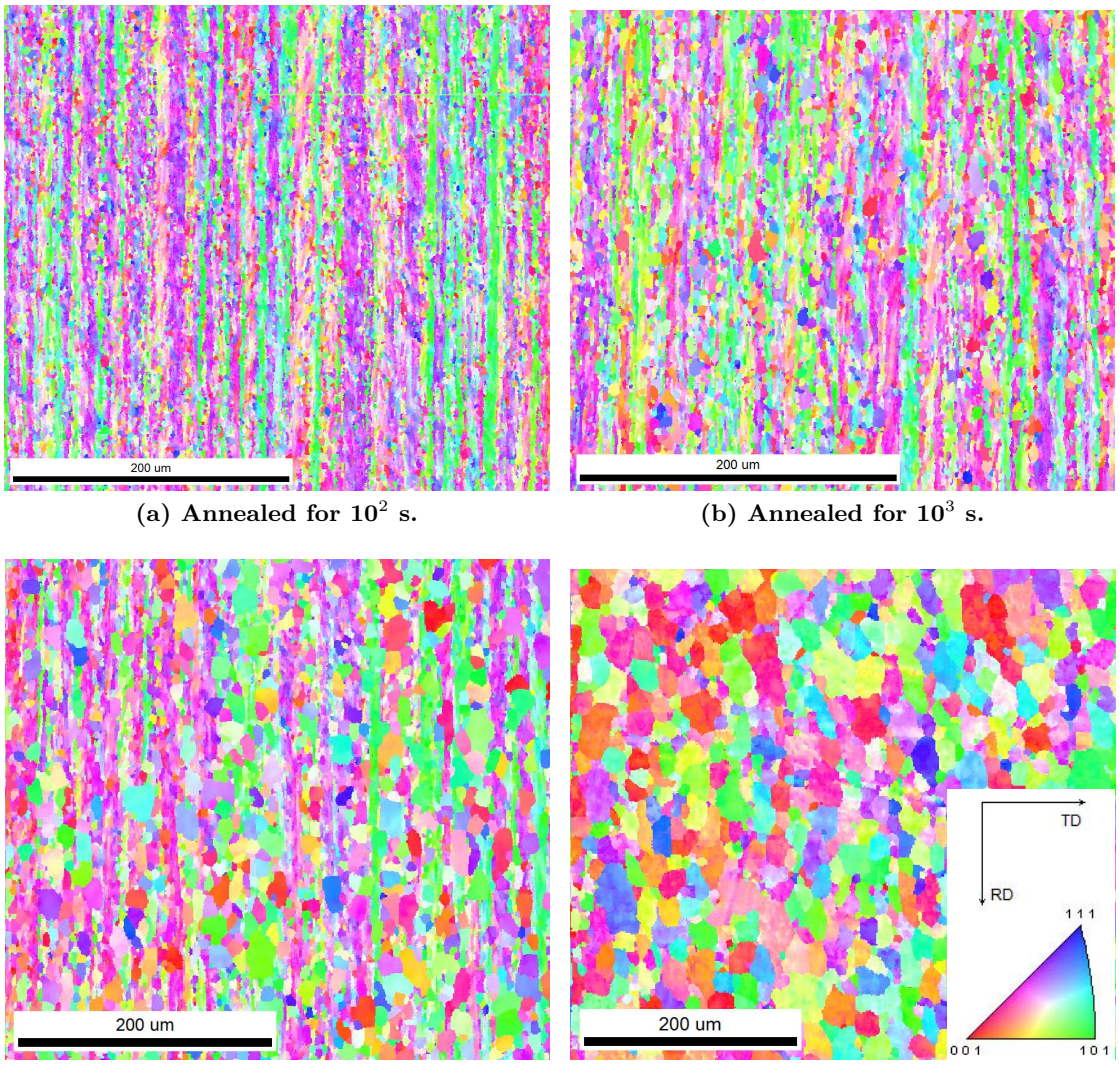

(a) Annealed for 10^2 s. **(b) Annealed for 10^3 s.**

(c) Annealed for 10^4 s. **(d) Annealed for 10^5 s.**

Figure 4.12: IPF from EBSD-maps of alloy B2 during annealing at 275 °C.

4.1.5 Recrystallized grain size

The grain size (area sections) in the recrystallized samples are given in Table 4.5, measured from EBSD-maps with the linear intercept method in the rolling direction. More than 300 grains were used for all these measurements. The grain size distributions are given in Appendix A. All the samples included should be fully or close to fully recrystallized according to the hardness measurements. However, alloy A2 annealed at 350 °C for 10^2 seconds did not look completely recrystallized according to the EBSD-maps, see Figure 4.13d. Only minor variations in the grain size for the same alloy are observed, and alloy A1 and A2 generally have larger grains than alloy B1 and B2.

Table 4.5: Grain sizes (area sections) in the recrystallized material. Time is the isothermal annealing time. The material included here should be fully recrystallized according to the hardness curves. Grain sizes are measured from EBSD-maps.

(a) Alloy A1

Temp. [°C]	Time [s]	Grain size [µm]
275	10^5	22.3
300	10^5	27.1
325	10^4	26.9
350	10^3	24.0
375	10^2	21.2

(b) Alloy A2

Temp. [°C]	Time [s]	Grain size [µm]
275	10^5	26.7
300	10^4	27.7
325	-	-
350	10^2	21.4
375	10^2	26.3

(c) Alloy B1

Temp. [°C]	Time [s]	Grain size [µm]
275	10^5	16.4
300	10^4	19.7
325	-	-
350	10^2	18.4
375	10	15.6

(d) Alloy B2

Temp. [°C]	Time [s]	Grain size [µm]
275	10^5	15.8
300	10^4	18.1
325	-	-
350	10^2	12.0
375	10^2	17.3

A selection of the IPF-maps from EBSD from which the grain sizes are calculated are given in Figure 4.13. The IPF of alloy A2 annealed at 275 °C for 10^2 seconds shows that this may not be fully recrystallized as large areas with small misorientations are present. This sample do also show another orientation to the left than to the right in the figure. To the left, the 001-orientations (the cube component) dominates, while the 101-orientations dominates to the right.

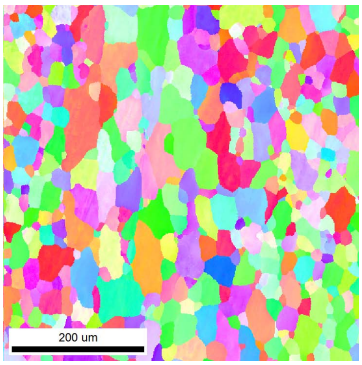

(a) Alloy A1 isothermally annealed at 275 °C for 10^5 s.

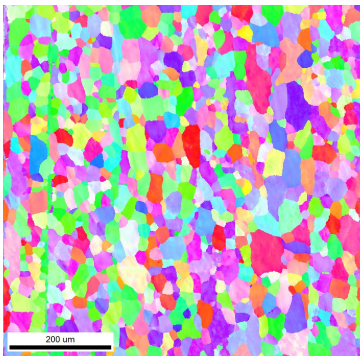

(b) Alloy A1 isothermally annealed at 375 °C for 10^2 s.

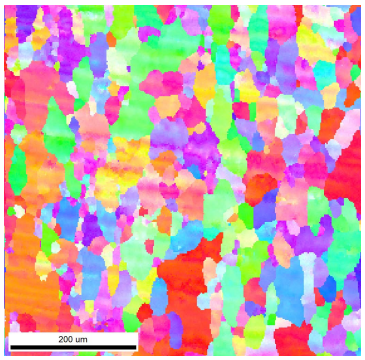

(c) Alloy A2 isothermally annealed at 275 °C for 10^5 s.

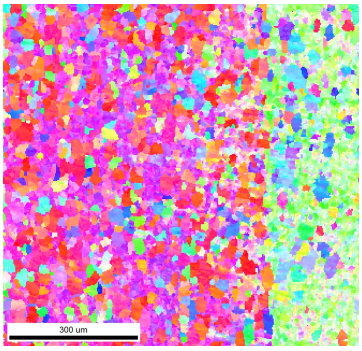

(d) Alloy A2 isothermally annealed at 350 °C for 10^2 s.

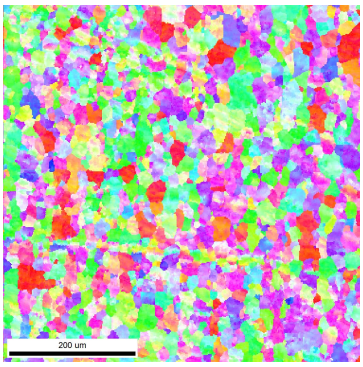

(e) Alloy B1 isothermally annealed at 275 °C for 10^5 s.

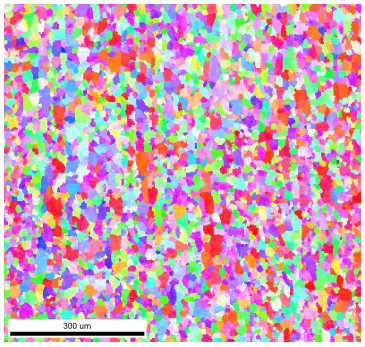

(f) Alloy B1 annealed at 375 °C for 10 s.

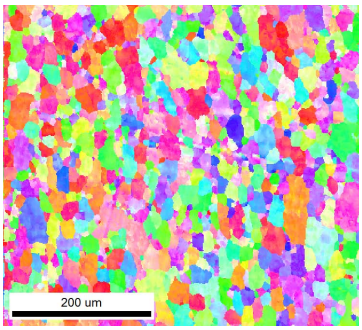

(g) Alloy B2 isothermally annealed at 275 °C for 10^5 seconds

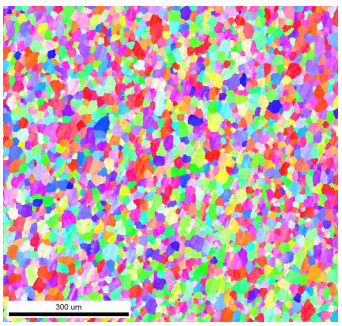

(h) Alloy B2 isothermally annealed at 375 °C for 10^2 seconds

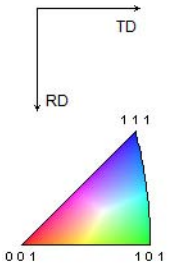

Figure 4.13: IPF from 100X to 150X EBSD-maps of the recrystallized material. Note the visible texture difference across alloy A2 in Figure 4.13d.

4.1.6 Grain growth

The grain sizes presented in Table 4.5 refer to the material which is just reached fully recrystallized state. For the highest temperatures, the grain sizes in the material annealed for 10^5 seconds were also measured, see Table 4.6.

Table 4.6: Grain size in the material that was annealed for 10^5 seconds for the highest temperatures.

(a) Alloy A1

Temp. [°C]	Grain size [µm]
300	-
325	27.3
350	29.0
375	34.3

(b) Alloy A2

Temp. [°C]	Grain size [µm]
300	28.2
325	-
350	30.9
375	34.2

(c) Alloy B1

Temp. [°C]	Grain size [µm]
300	21.4
325	-
350	20.7
375	22.1

(d) Alloy B2

Temp. [°C]	Grain size [µm]
300	17.2
325	18.2
350	19.8
375	21.4

For better illustration of the grain growth, the grain sizes in the material which is just the fully recrystallized state compared to the grain sizes in the material annealed for 10^5 seconds is given in Figure 4.14. Annealing from 10^4 to 10^5 seconds at 275 °C gives almost no difference in grain size. For alloy B2, the measured grain size is lower for the longest annealing time at this temperature. Some grain growth is observed at the other annealing temperatures.

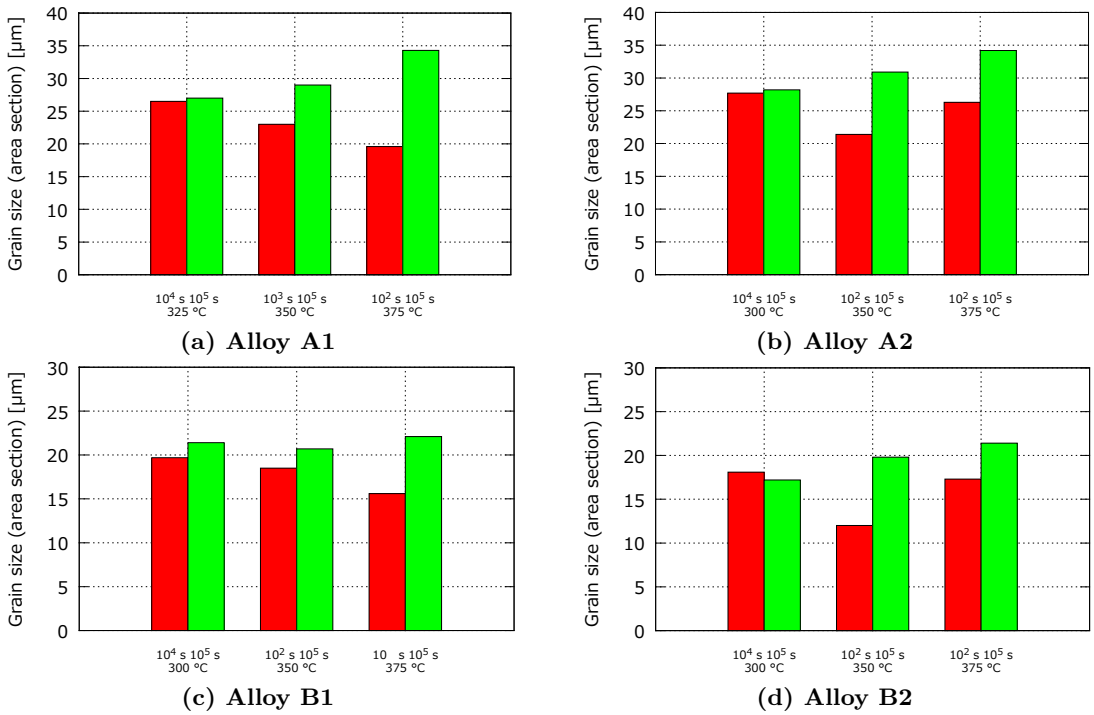

(a) Alloy A1 **(b) Alloy A2**

(c) Alloy B1 **(d) Alloy B2**

Figure 4.14: Overview of the grain growth during further annealing after complete recrystallization.

4.1.7 Global texture

Texture plots as ODFs of the recrystallized material are given in Figure 4.15 and 4.16. The material in Figure 4.15 is annealed at 275 °C for 10^5 seconds, i.e. they have just reached recrystallized state. Only alloy A1 and B2 are measured at this annealing temprature. In Figure 4.16, the material is annealed for 375 °C for 10^5 seconds, which means subsequent grain growth has occured.

The maximium intensity of the strongest textures in the material annealed at 275 °C is just above 8. The cube, S and copper texture components are all represented. Few differences between alloy A1 and B2 are observed, although the S and copper components are a bit stronger in alloy A1.

For the material annealed at 375 °C for 10^5 seconds, strong cube and copper components are present. Also, peaks corresponding to the S components are strong, especially in Alloy B1. The texture of alloy A2 is a bit different from the other alloys. It is about as strong as the other, but the cube peaks are more shifted toward the middle, i.e. rotated around ND. The R component is more clearly present, which is observed nearly at the same position where the S is present in the other alloys, somewhat shifted down and to the left.

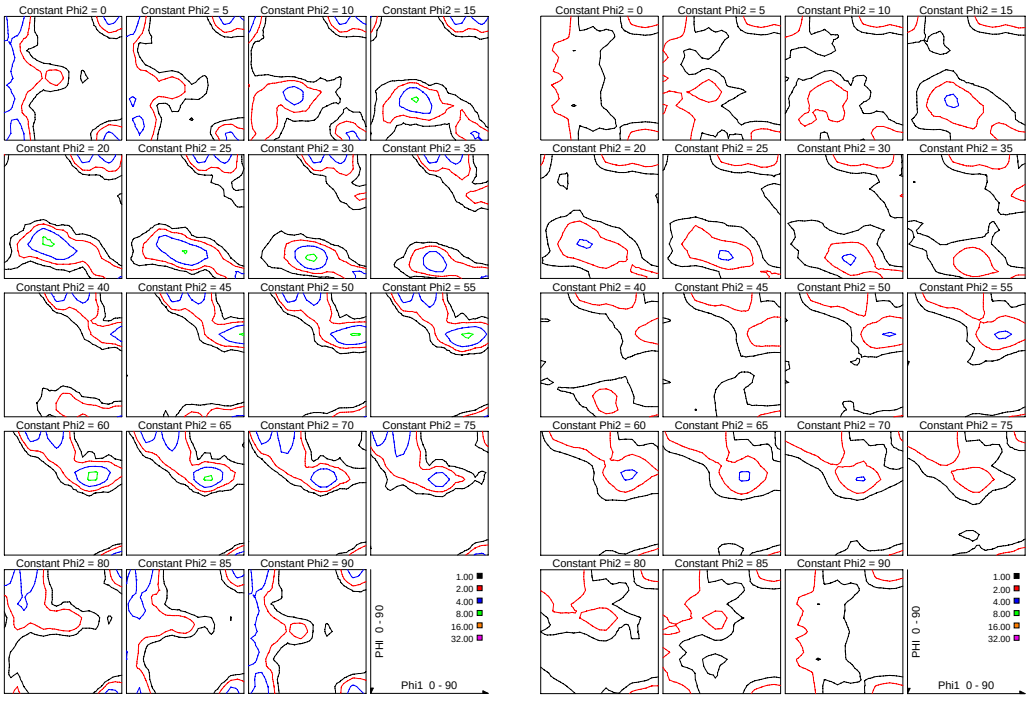

(a) Alloy A1. $f_{max} = 7.13$ **(b) Alloy B2.** $f_{max} = 4.48$

Figure 4.15: ODF of the alloys, annealed at 275 °C for 10^5 seconds. Note that the lines with the same colour has the same intensity for all figures. Volume fraction of the grains of certain orientations are given as f_{max}.

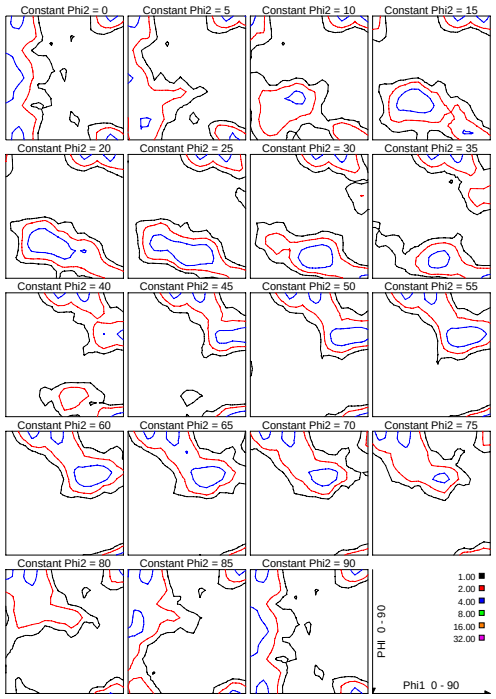

(a) Alloy A1. $f_{max} = 6.82$

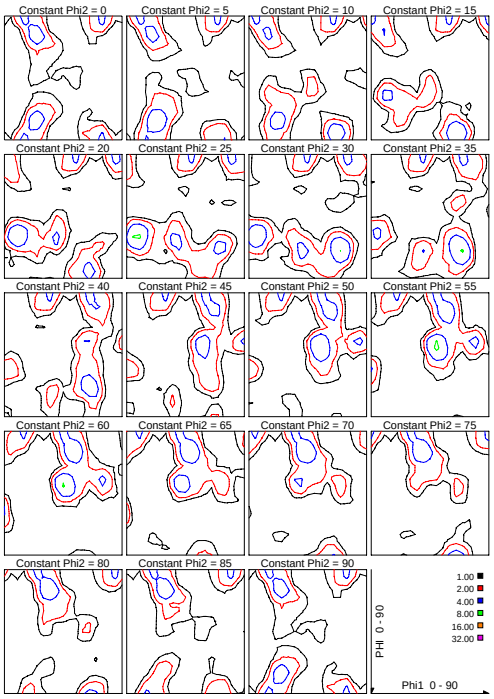

(b) Alloy A2. $f_{max} = 8.90$

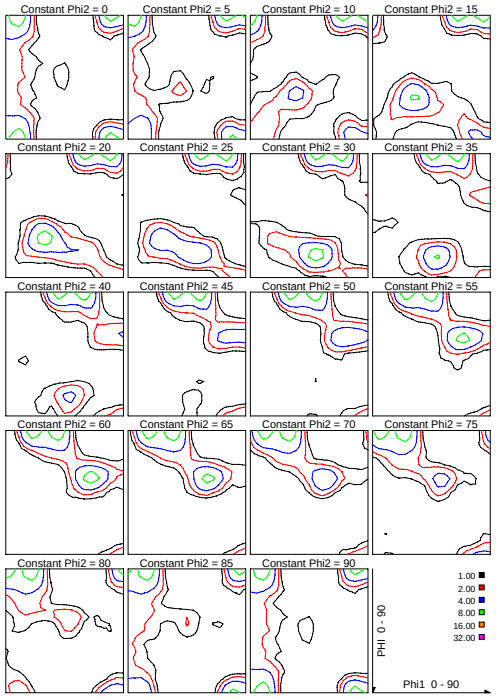

(c) Alloy B1. $f_{max} = 10.17$

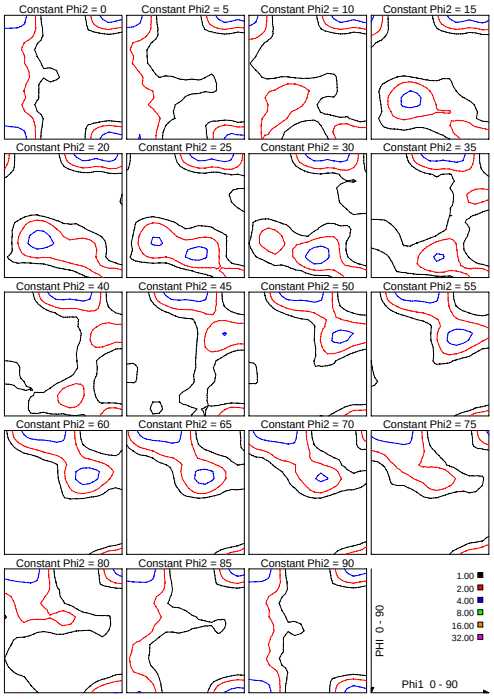

(d) Alloy B2. $f_{max} = 5.11$

Figure 4.16: ODF of the alloys, annealed at 375 °C for 10^5 seconds. Note that the lines with the same colour has the same intensity for all figures. Volume fraction of the grains of certain orientations are given as f_{max}.

4.2 Modelling

To characterize the recrystallization kinetics in terms of the different cases, the Avrami exponents n in the JMAK equation (see Equation 2.6) are found as the slope to the curve $\ln(\ln(\frac{1}{1-X(t)}))$ plotted versus $\ln(t)$. These plots are called Avrami plots, and are given in Figure 4.17. The experimental values for fraction recrystallized are based on the hardness curves in Figure 4.7-4.10.

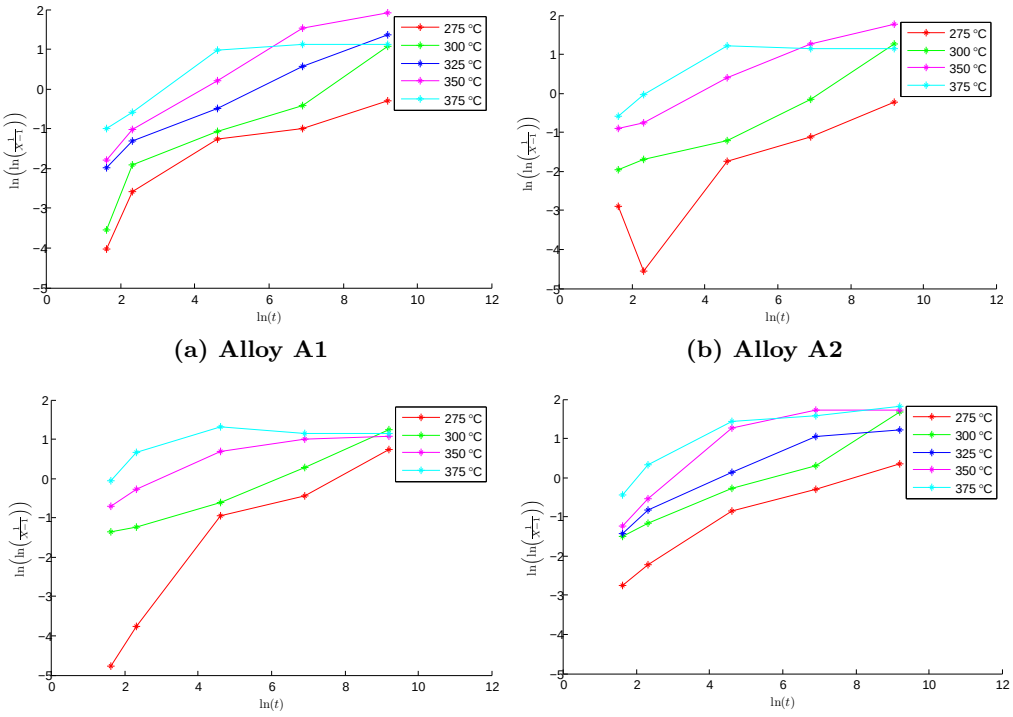

(a) Alloy A1 **(b) Alloy A2**

(c) Alloy B1 **(d) Alloy B2**

Figure 4.17: Avrami plots of the four alloys based on experimental hardness curves.

The slope of these curves is found with linear regression and is given in Table 4.7. All values are generally lower than 1, most of them around 0.3-0.4, which is about 10 times lower than the recrystallization mechanisms of site saturatution and Johnson Mehl.

Table 4.7: The avrami exponent n for the softening curves for the four alloys found by linear regression. The fraction recrystallized is based on the mechanical properties.

(a) Alloy A1

Temp. [°C]	n
275	0.5
300	0.6
325	0.4
350	0.5
375	0.3

(b) Alloy A2

Temp. [°C]	n
275	0.4
300	0.4
325	-
350	0.4
375	0.3

(c) Alloy B1

Temp. [°C]	n
275	0.7
300	0.3
325	-
350	0.2
375	0.2

(d) Alloy B2

Temp. [°C]	n
275	0.4
300	0.4
325	0.4
350	0.4
375	0.3

5 Discussion

The main goal of this work has been to characterize of the softening behaviour of the four alloys with respect to variations in mechanical properies, texture and recrystallized grain size. The effect of different amounts of Fe and Si, the ratio between them and the total content of alloying elements will be discussed in this chapter.

5.1 Initial material

The as-cast material shows that alloy A1 has larger and more elongated grains than the other three alloys. This is probably due to uniaxed growth during the DC casting. The descending casting ingot will create a pool of liquid metal, and columnar grain growth normal to the freezing front can occur. The EBSD-maps of the other alloys shows that they are more equiaxed. The grain size of the as-cast (as well as the the homogenized) material may be subject to large variation throughout the casting ingot and the rolling slab, and both columnar and equiaxed microstructures may be present in all alloys. The grain size results should therefore only be taken as an approximation.

Smaller grain size after homogenization was observed in alloy A1 and B2. The reason for this may be an inhomogenous grain structure throughout the casting ingot. Even though all samples investigated in RD-ND plane both before and after homogenization, they were not from the same position on the rolling slab. The grain size distribution for alloy A1 in the homogenized material (see Figure A.1b) shows that the distribution is rather inhomogenous, and a greater number of grains should be measured for more correct values. The same alloy in the as-cast state (see Figure A.1a) shows that the largest grains dominates, and if more grains were included, the average size would possibly be even larger.

5.1.1 Alloying elements

An interesting part of this work is to study the effect of the Fe-Si ratio in the different alloys. In words, alloy B1 has ten times more Fe than Si, alloy A1 has three times more Fe than S, while there is just above three times more Fe than Si in alloy B2. The amount of Fe and Si are the same in alloy A2.

Most of the Fe content in the alloys is in the form of intermetallic phases seen in Figure 4.2, since the solubility of Fe is low. Aluminium can dissolve much more Si, since they are much alike in size and Si fits well in the vacancies. It is then reasonable to assume that if an alloy contain more Si, less Fe is expected in solid solution as the vacancies already is filled with Si. Alloy A2 and B2, which both contain 0.15 wt% Si, should then contain less Fe in solid solution and more of the Fe-rich particles.

This is also observed in the estimation of the area fraction of particles. Alloy A2 and B2, even though they contain more alloying elements in total compared to alloy A1 and B1 respectively, contain slightly less particles. The reason for this must be that the Si-atoms, which are easier to dissolve, forces Fe to form intermetallic particles. This is the particles which are large and possible to observe in the SEM images (Figure 4.2), and

they are denoted constituent particles and cannot be broken down by heat treatment alone.

Work done on exactly the same alloys in the as-cast state concluded that only one type of particle is present [40]. If the level of Si is low (0.05 and 0.15 wt%), regardless of Fe content, the particles appeared to be Al_3Fe, Al_6Fe or Al_mFe. If this is assumed to be correct, the Matthiessens rule can be used to calculate the amount of Fe in solid solution from electrical conductivity measurements. The results from this, given in Table 4.2, shows that alloy A1 has more Fe in solid solution than alloy A2 and alloy B1 has more than alloy B2. This supports the assumption that more Si leads to more Fe in particles.

Due to the long holding time at 600 °C during homogenization, it is, according to previous work on the same alloys, expected that any eventual dispersoids will dissolve. No precipiation will occur during the following cooling sequence. The increase in electrical conductivity from as-cast to homogenized state is most likely due diffusion of Fe and Si to the constituent particles [41].

5.1.2 Abnormal grain growth of alloy A2

Alloy A2 was homogenized just like the other alloys, but the characterization of the microstructure showed that this alloy has grains sizes in the order of several mm after homogenization. Hence, the texture and softening behaviour are affected and may not show the typical results. The much stronger texture in alloy A2 is most likely due to the large grains from the initial state.

The process when a few grains grow excessively and consuming other grains is called abnormal grain growth and have occured during homogenization. The high temperature during homogenization gives enough ene for the grains to reduce their boundary energy through grain growth. Homogenization at 600 °C for 24 hours is a rather long time and high temperature. Since it only happened to one of the alloys, some other factor than the high temperature alone must have triggered the abnormal grain growth.

Since the abnormal grain growth is observed near the surface of the rolling slab, it is reasonable to assume that it may have been triggered by som sort of surface effect, e.g. like a region with large deformation or impurities from the cutting process. Since the other alloys underwent exactly the same cutting, this assumption seems to be invalid.

The driving pressure for abnormal grain growth comes from the orientation dependence of the surface energy. The velocity of abnormal grain growth is predicted to be inversely proportional to the sheet thickness, and is therefore often observed in thin sheets. Work done on thin sheets suggests that abnormal grain growth occurs if normal grain growth is inhibited by the free surfaces [42, 43]. However, in this case the material is far from thin sheets.

It has been demonstrated that strong presence of single texture components in a fine-grained recrystallized material often leads to abnormal grain growth during further annealing at high temperatures [44]. Since the grain size is large and the texture is random in this case, something else must have caused the abnormal grain growth.

Second-phase particles will prevent growth above a limiting size if the Zener drag part in Equation 2.21 becomes large enough. It is in alloy A2 the amount of particles are smallest, and this may explain why it only happened to only this alloy. However, since the level of particles is about the same as in alloy A1, this factor may not be the reason. In this case, the observed phenomena is therefore probably incidental, and abnormal grain growth in these alloys is a stochastic character.

5.1.3 Deformed material

The images from the opical light microscope in Figure 4.5 shows that all the alloys except A2 exists in the form of the typical elongated band structure with numerous high angle grain boundaries. The much larger initial grain size of alloy A2 is the reason for its special deformed structure. A closer look on the deformed microstructure shows that there are regions of sharp orientation gradients inside the large grain. The grains may have split during deformation and are seperated by the bands known as transition bands. These regions may also work as good nucleation sites.

The deformation texture of the alloys (see Figure 4.6) contains the most typical components like brass, S and copper. The cube orientation is not visible in either on the ODFs, which is expected since deformation to high strains reduce the cube component [28]. As mentioned in Chapter 2.5.2, the presence of the S orientaion gives the cube good growth conditions.

For a better illustration of the mechanical properties of the deformed and the annealed material, these values are graphically presented in Figure 5.1. There are little differences in hardness between the alloys. Alloy A1 and B1 are somewhat softer than alloy A2 and B2 respectively, probably due to less Si in solid solution. The large initial grain size in alloy A2 do not seem to have affected the hardness values much, which indicates that strain hardening contributes more to the strength than the grain size.

5.2 Softening behaviour

One of the most remarkable observations from the hardness curves (Figure 4.7-4.10) is that the softening process for the alloys is rather slow compared to similar work done previously by Furu [45], Sæter [46] and Tangen [47]. In Figure 5.2, the softening curves for these alloys are given, which are similar to the alloys in this work. Work done by Sæter shows that a commercial pure aluminium alloy with 0.17 wt% Fe and 0.05 wt% Si deformed to ϵ=2.6, which is very similar to alloy A1, is completely recrystallized after 10^3 seconds after annealing at 280 °C [46]. Furu studied an alloy containing 0.43 wt% Fe and 0.09 wt% Si deformed to ϵ=3, and less than 0.01 wt% Fe in solid solution, which may be compared to alloy B1 and B2, and found that it was completely recrystallized after 10^3 seconds after annealing at 300 °C [45]. This alloy is denoted "Furu 2" in Figure 5.2. The graph denoted "Furu 1" contained 0.02 wt% Fe in solid solution, and recrystallized later.

In this case, alloy A1 is annealed at 300 °C is fully recrystallized after 10^4 seconds. It was speculated that one possible reason for the slow softening could be the large initial

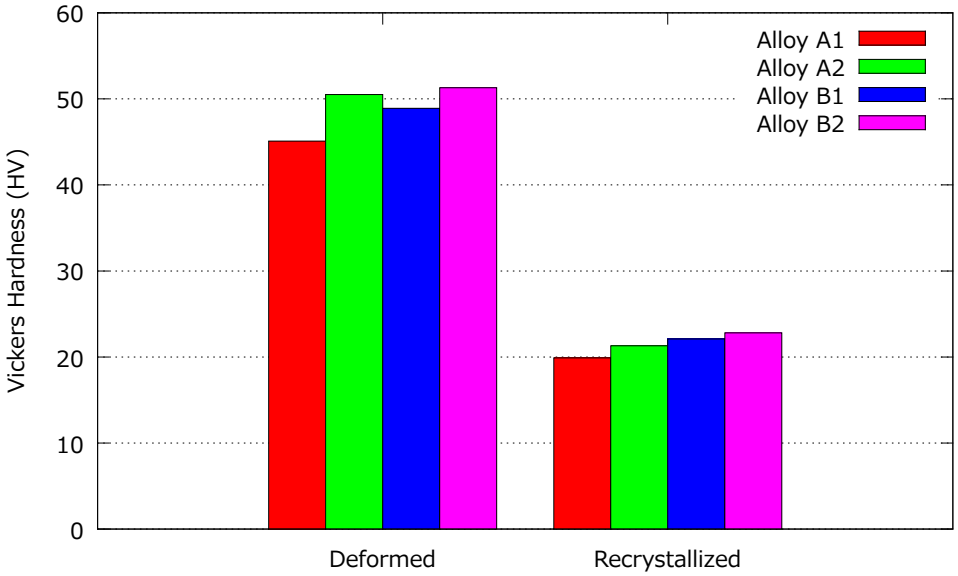

Figure 5.1: Histogram showing Vickers hardness for the deformed and the recrystallized material.

grain size. A large grain size before deformation will result in fewer high angle grain boundaries in the deformed material where recrystallized grains have the conditions to nucleate. The nucleation frequency may hence be lower due to both cube sites and other strain induced nucleation.

To investigate if this was correct, the initial grain size of alloy A1 was reduced according to the procedure given in Chapter 3.2.3. The grain size was found from EBSD-maps to be 38.2 µm, which is 27 % of the origianal initial grain size of 139.7 µm. An EBSD-map showing the microstructure and the grain size distribution is given in Figure C.1 and C.2 in Appendix C. After further cold rolling to a strain of 2.6, the softening behaviour during isothermal annealing was characterized with hardness measurements.

The Vickers hardness of alloy A1 with finer grain size during isothermal annealing at 300 °C are shown in Figure 5.3, and it follows more or less exactly the same development as the original alloy. Hence, no further investigation of alloys with finer grain size was executed. At this level, the difference in grain sizes in the initial material may therefore not be of great importance. The grain boundary nucleation mechanism may in this case not be as important as the other mechanisms like cube and PSN.

The softening behaviour of alloy A2, which initially have very large grains, recrystallized more or less in the same manner with respect to kinetics as the other three alloys. The IPFs of the recrystallized material (Figure 4.13c-4.13d) shows that the grains nucleate inside the area with little amount of old grain boundaries. This also confirms that these alloys do not need a large amount of the high angle grain boundaries to nucleate recrystallized grains. The grains may have nucleated with the PSN mechanism or at bands inside the large grains (transition bands).

The log-linear softening curves observed, for alloy B2 in particular, may be explained

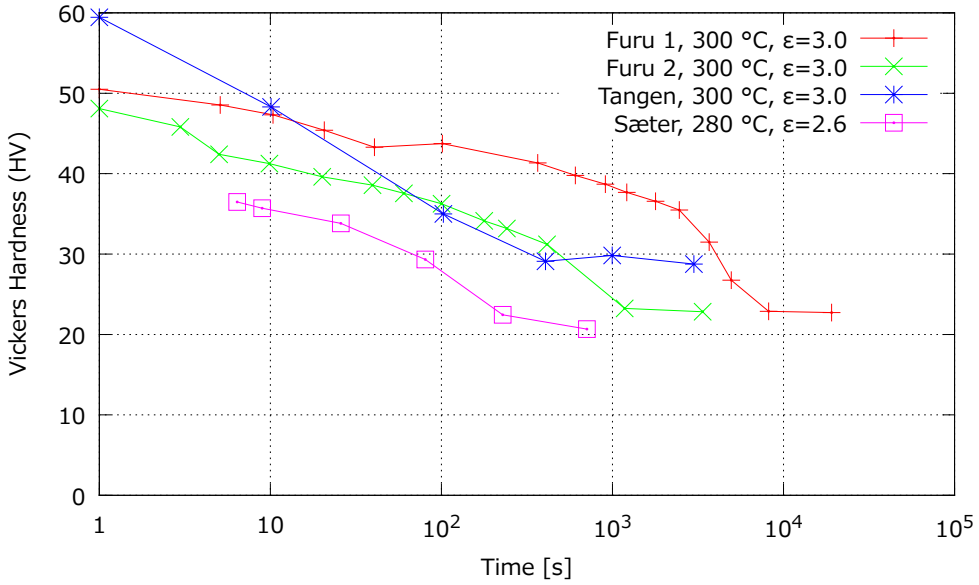

Figure 5.2: Vickers hardness against annealing time from previous work on alloys similar to alloy A1 [45, 46, 47].

with the fact that classic recrystallization with nucleation and growth to some extent are absent, and so-called continuous recrystallization is the case. In this case, subgrain growth is dominating the entire softening process. To find out if this is the case, the evolution in texture can be studied further. For new deformation-free grains to nucleate and grow, i.e. the so-called discontinuous recrystallization, the nuclei must have a size above a certain critical value, given in Equation 2.15. This gives rise to clear recrystallization textures since some orientations grows faster than others, as explained in Chapter 2.5.2. If the texture of the soft material (the material with hardness values of the fully recrystallized) are similar or almost similar to the recovered state, the case of continuous recrystallization might be have been the case.

The IPFs for alloy B2 during annealing at 275 °C (Figure 4.12) can be compared to alloy A1 (Figure 4.11) and give some indications of how the recrystallization texture evolved. Both alloys are slow due to the low annealing temperature. The changes in the microstructure from 10^4 to 10^5 seconds in much more drastic in alloy A1, where new grains have nucleated and grown. Alloy B2 for the same annealing period are more dominated by the growth of grains already nucleated. However, it shows clear indications also in this alloy new grains with high angle boundaries have nucleated and grown, but on an earlier stage than in alloy A1. Both alloys seem to have been through discontinuous recrystallization from the IPFs.

From the theory of recrystallization textures, alloy A1 should contain more of the typical cube, R and P orientations than alloy B2 in the recrystallized state if the recrystallization is more of the discontinuous character. From the ODFs (Figure 4.16), the typical deformation orientaions copper and S are still present in the recrystallized state for both alloys. However, the ODF for alloy A1 indicates that the cube are stronger in this alloy than in alloy B2. This component, together with the S component, are observable in

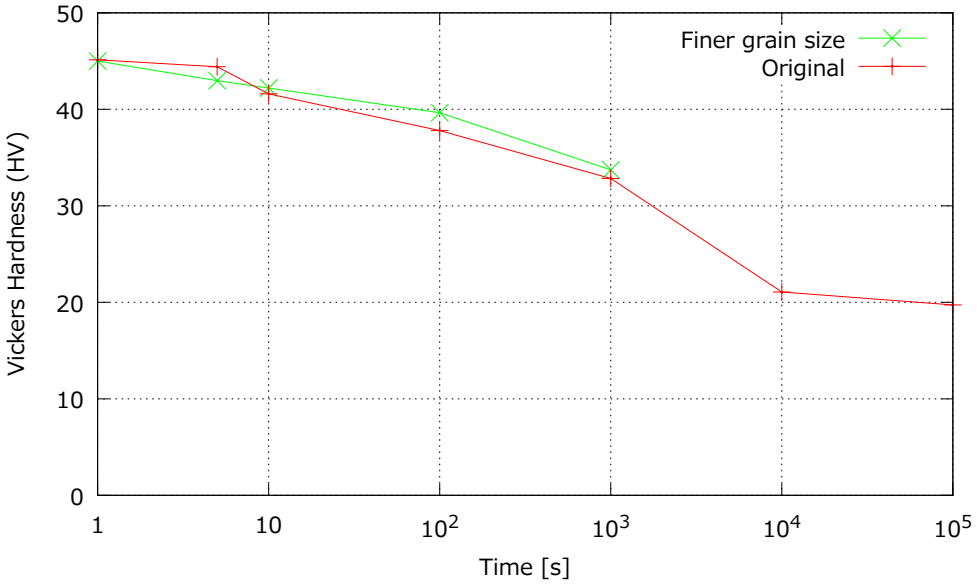

Figure 5.3: Vickers hardness versus annealing time at 300 °C isothermal annealing for the original alloy A1 and the alloy with finer grain size. Almost no change in softenig kinetics when initial grain size is approximately 30 % of the original.

alloy A1 while they are weaker or not present at all in alloy B2, as the details from the ODFs shows (see Figure 5.4). The texture in alloy A1 is stronger than the texture of alloy B2, and this may support the observations of a more continuous recrystallization of alloy B2.

A slight shift (∼10°) to the left of the S peak towards the R peak would indicate a more discontinuous recrystallization [29]. When comparing the ODFs of the deformed material and of the annealed at 275 °C, the peaks seems to be at the same position (see Figure 5.5), which do indicate that the softening is more dominated by recovery. Only alloy A2 annealed at 375 °C for 10^5 seconds, which in this work is a special and not representable case, have a clear R peak present. Here, the R peak was present in the deformed material as well.

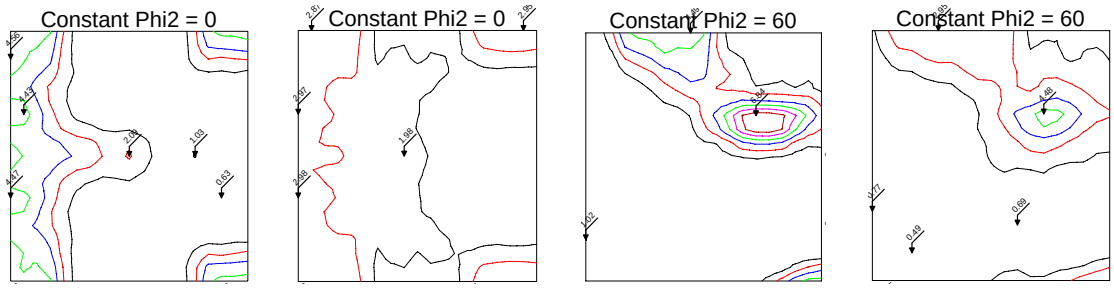

(a) Alloy A1 **(b) Alloy B2** **(c) Alloy A1** **(d) Alloy B2**

Figure 5.4: A closer look at the ODF for the material annealed at 275 °C for 10^5 seconds shows stronger peaks for cube, R and P in alloy A1 than in alloy B2.

Since generally more PSN mechanism is accompanied with random texture and weak

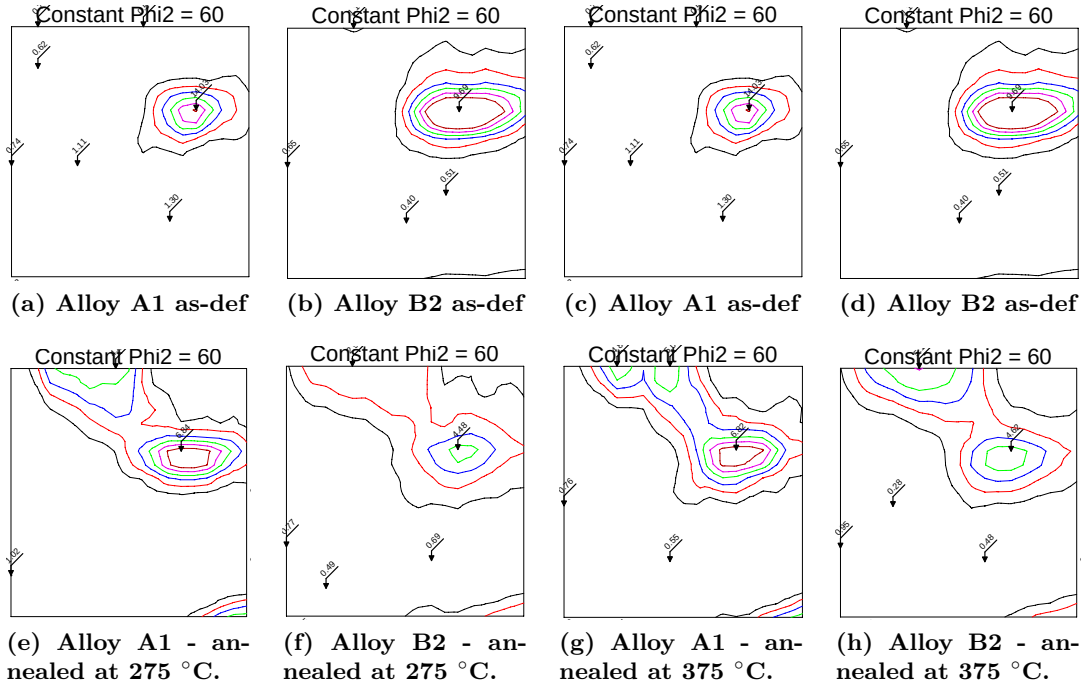

(a) Alloy A1 as-def **(b) Alloy B2 as-def** **(c) Alloy A1 as-def** **(d) Alloy B2 as-def**

(e) Alloy A1 - annealed at 275 °C. **(f) Alloy B2 - annealed at 275 °C.** **(g) Alloy A1 - annealed at 375 °C.** **(h) Alloy B2 - annealed at 375 °C.**

Figure 5.5: Sections in the ODFs of the alloys after deformation compared to after 10^5 s annealing. The S peaks at the deformed material (deformed state given twice for better comparison) are still present in the annealed material. Only in alloy A1 annealed at 375 °C, the peak has slighly shifted towards the left (the R orientation).

preference for the P and the ND-rotated cube orientations, these components should be present in the alloys. The P orientation is not visible in the ODFs for the recrystallized material. However, the cube orientation seems to be rotated around ND as the peaks are slightly shifted towards the center (i.e. towards ϕ_1=45°), which indicates that PSN has been an important nucleation mechanism.

Since the IPFs shows the classical nucleation and growth, as well as the deformation texture is partly replaced by different textures, the recrystallization seems to be of discontinuous nature. The recrystallization process seems to be starting after a incubation time, and together with a slow recovery, the softening curve shows a linear decrease in hardness on a logarithmic time scale.

Another observation on the softening curves is the slight increase in hardness for alloy A1 and A2 at the early stages of annealing at 275 °C. This effect is also observed for AlMn alloys and is probably due to clustering of the solute atoms [46]. At the higher annealing times, this effect is not observed, most likeley due to faster recovery and recrystallization. This most eminent for alloy A2 from 5 to 10 seconds annealing time. This alloy have more Si in solid solution than alloy A1 and B1, which may indicate that is is the solved Si which forms the clusters. There is no sign of this effect in alloy B2, possibly due to that more Fe stops the Si to forms the clustures.

5.2.1 Concurrent precipitaion

The alloys in this work has generally low contents of alloying elements, and the rather long cooling at the homogenization was done in order to avoid alloying elements in supersaturated solid solution. Concurrent precipitaion is difficult to observe from the electrical conductivity measurements due to very low levels of elements in solid solution. As it is difficult to determine from the results if concurrent precipitation have happened at all, it is even more difficult to determine if it is the Fe or the Si which have precipitated, as the supersaturated Si may also be subject to concurrent precipitaion. The largest part of the increase in electrical conductivity is mostly due to the reduction in dislocation density as the material is annealed, since almost all the electrical conductivity values in the annealed material do not exceed the values of before deformation. Some observed correlations between the softening curves and the conductivity curves can support to this. Where the material recrystallizes and the hardness drops is also where the largest increase in electrical conductivity is found. In addition, the conductivity curves levels out when the alloys reaches fully recrystallized state.

However, it is possible to find some small tendencies in the results that may indicate concurrent precipitation. Alloy A1 and B2 do have higher conductivity values in the material annealed for the longest times at the lowest temperatures. This indicates that some precipitation may have happened. Alloy B1 and B2 have more Fe in solid solution (see Table 4.2 compared to alloy A1 and A2, respectively. As it is assumed that all Si is in solid solution, the total amount of elements in solid solution is higher in alloy A2 and B2.

The electrical conductivity values after complete recrystallization shows that these alloys do not precipitate more than alloy A1 and B1, which means that precipiation of Si may not be present. Still, the curves for lower temperatures for alloy A2 and B2 are increasing for the longest annealing times slightly more than the other two.

From the measurements prior to annealing, it is found that these alloy B1 had slightly more Fe in solid solution than alloy B2, but the difference was only 0.01 wt%. This is expected due to the limited solubility of Fe. One explanation for the indications that concurrent precipitation may have happened more extensively in alloy B2 than in alloy B1 is that it is easier for Fe to precipitate with more Si present. The dissolved Fe atoms may be less stable with three times more Si already solved in the lattice, and this may increase the precipiation rate of Fe-rich particles. Another explanation is that precipitaion of Si is actually happening. The solubility of Si decreases with lower temperature, and at the lowest annealing temperatures the driving force may be high enough for Si to precipitate.

The fact that alloy B2 shows the highest increase in electrical conductivity during annealing, and have the slowest recrystallization, the pinning pressure from dispersoids could be the reason for the slow recrystallization of this alloy. However, the differences in electrical conductivity are very small, and concurrent precipitation is most likely of little importance due to the low content of alloying elements.

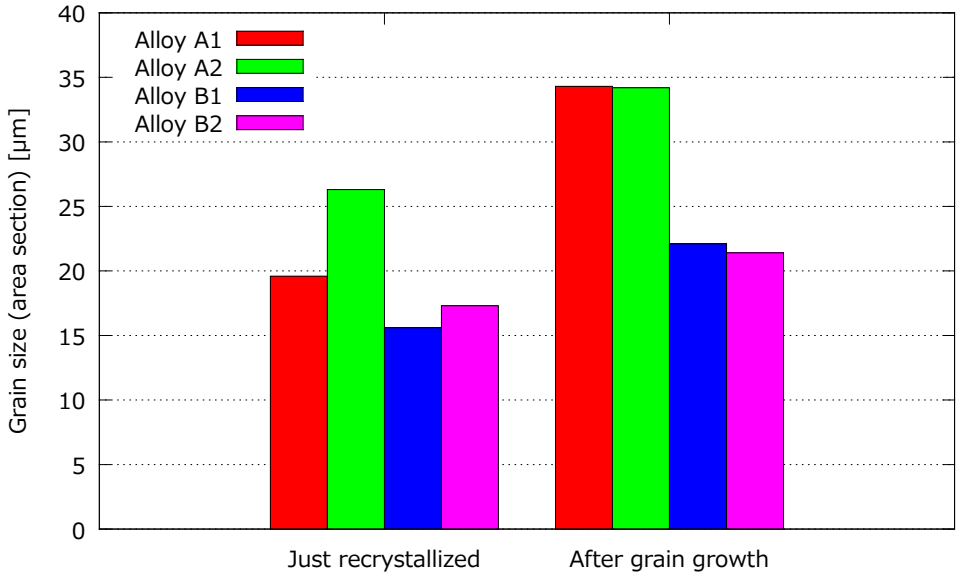

Figure 5.6: Histogram showing the recrystallized grain size. "Just recrystallized" are the alloys annealed at 375 °C after 10^2 seconds for alloy A1, A2 and B2 and after 10 seconds for alloy B1, and "After grain growth" are the material annealed at 375 °C for 10^5 seconds.

5.2.2 Recrystallized grain size

To illustrate the recrystallized grain size, a graphical representation given in Figure 5.6. The bars labelled "Just recrystallized" are the grain sizes to material which just has reached recrystallized state after annealing at 375 °C, i.e. after 10^2 seconds for alloy A1, A2 and B2 and after 10 seconds for alloy B1. The bars labelled "After grain growth" are the material annealed at 375 °C for 10^5 seconds.

The recrystallized grain sizes of alloy A1 and A2 are larger than the of alloy B1 and B2. One possible reason for this is that the larger amount of constitutent particles means more PSN sites and therefore more recrystallized grains. If PSN sites is assumed to be the only nucleation mechanism and site saturation kinetics are assumed, then the grain size can be approximated by:

$$D_N = N_d^{-1/3}, \tag{5.1}$$

where D_N is the grain size and N_d is the number of particles capable of acting as a nuclei. The fact that alloy B1 and B2 has a smaller grains size shows how important the particles are for nucleation. The higher amount of elements in solid solution may also have contributed to a smaller grain size in alloy B1 and B2, since they slow down moving grain boundaries by the solute drag. The highest Zener drag comes from the smallest particles, so the larger amount of large particles in alloy B1 and B2 is probably not a part of the explanation.

The fact that the recrystallized grain size are as large as they are, about 18 µm in alloy A1 and A2 and about 25 µm for alloy B1 and B2, can also be used to turn down that the alloys underwent a continuous recrystallization. In a case of continuous recrystallization

on high purity aluminium during annealing after 98% deformation, the grain size was found to be an average 6 μm [31]. If continuous recrystallization was the case in this work, the final grain size would probably be much finer.

5.2.3 Grain growth following recrystallization

The grain growth observed is larger in alloy A1 and A2 than alloy B1 and B2. One explanation may be that a larger amount of particles in these alloys acts with a pinning pressure on the grain boundaries, just as the effect observed during recrystallization of new grains. It is dispersions of small particles which acts with the highest retardig force. As the level of dispersoid and concurrent precipiation in the alloys is assumed to most likely be low, the difference in grain growth might be due to the solute drag from the alloying elements.

The ODFs of the alloys annealed at 375 °C for 10^5 seconds shows much of the same texture components compared to the alloys annealed at 275 °C for 10^5. Since both of these alloys are completely recrystallized, the minor changes in the texture during the grain growth phase is expected.

5.3 Modelling the softening kinetics

As the Avrami plots in Figure 4.17 shows, the Avrami exponent n for the curves deviates much from the site saturation case where n=3 and the Johnson Mehl case where n=4. All of the softening curves has an Avrami exponent of around 0.5. This means that the kinetics do not behave according to the classical models. The notable dip in the Avrami curve for alloy A2 at 275 °C is due to the increase in hardness at the shortest annealing times.

A weakness with the Avrami plots may be that they are, in this case, based on the hardness measurements. Hardness is related to the yield stress, but because of the complex relationship between strength and microstructure it may be difficult to interpret mechanical properties changes in terms of microstructural events. However, five hardness measurements was done on different places of the samples to minimize effect from a heterogenous microstrucure.

The Avrami exponent varies depending on the function for growth rate ($G(t)$ in Equation 2.13). The growth rate and the nucleation frequency is in the case of both Johnson Mehl and site saturaion assumed to be constant. The values for n, which do not fit neither of these cases, is meant for characterizing the recrystallization part of the softening curve with the large drop in strength. The softening curves in the work is dominated by recovery and a slow recrystallization, which means the the Avrami exponoents do not make sense.

As alredy pointed out, one reason for the slow softening, i.e. a dominating recovery, may be the Zener drag from precipitates. It should be noted that the expressions used in Alsoft to calculate subgrain growth and dislocation density, given in Equation 2.11 and 2.10, do not directly take care of the pressure from the particles. Subgrain growth

is treated somewhat similar to normal grain growth with a driving pressure on subgrain boundaries inversely proportional to the subgrain size.

To illustrate this, som principial simulations done with Alsoft is given in Figure 5.7a. These simulations are taken from the the project work during fall 2011 [48]. If the Zener drag is set to be very high, as increasing fractions of the driving pressure (see Chapter 2.4.2 for more information), the effects become visible as the effective dirving force for recrystallization becomes very low. The behaviour of the curve where the Zener drag is

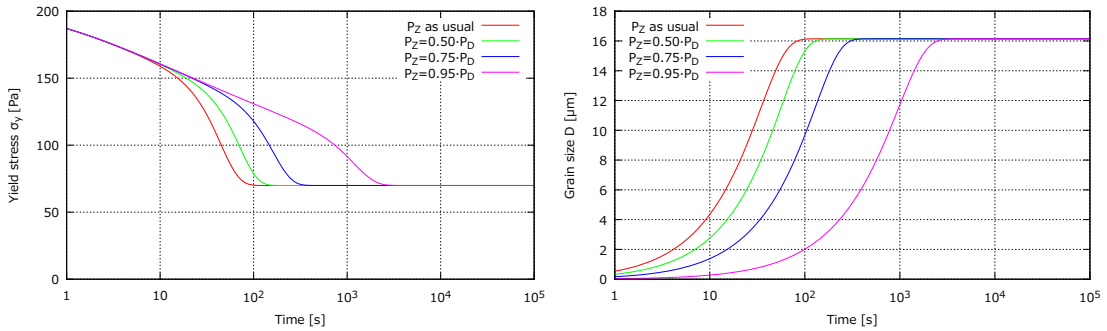

(a) Yield stress versus time. **(b) Grain size versus time.**

Figure 5.7: Simulated softening curves, where the Zener drag as fractions of the driving pressure is compared to the classical approach.

set to 95% of the driving force is more similar to the observed softining behaviour in this work. Even though these simulated curves shows a case where there is almost no driving force for recrystallization, the material recrystallizes in the end when the driving force are large enough. After recrystallization eventually is complete, the grain size reaches the same level as in the other cases, which is also more or less the case for the alloys in this work. This is given in Figure 5.7b.

A combination of time dependent nucleation and a slower grain growth due to precipitates seems to be needed for the better modelling of these alloys. A model with time dependent nucleation could include a incubation time for the start of recrystallization.

5.4 Further work

A softening behaviour without a clear transtion from recovery to recrystallization leads to difficulties when it comes to modelling. To model softening of commercially pure aluminium alloys like this, where the recovery part seems to be more dominating, time dependent nucleation of recrystallized grains needs to be taken into account. More investigations of the growth rate where pre-existing particles plays a role may also be needed. In this work, a characterization of the evolution of the subgrain structure has not been carried out. Subgrain growth and recovery kinetics may be subject to further investigations, which means more detailed EBSD-mapping to identify where and when the recrystallized grains nucleate.

In addition, the cause that triggered the abnormal grain growth in the rolling slab during homogenization at 600 °C is still an open question. Grain growth during homogenization

may be further studuied.

6 Conclusions

The softening behaviour with respect to mechanical properties, texture and grain size in four different commercially pure aluminium alloys has been investigated. The main objective was to study the effect of different amounts of Fe and Si.

- All alloys reached fully recrystallized state after 10^4 seconds isothermally annealing at 300 °C, while alloy B1 and B2 are slightly faster at the higher temperatures. Alloy B1 and B2 begins to recrystallize before alloy A1 and A2 due to more particle stimulated nucleation (PSN) at the large Fe-rich particles. Alloy B1 and B2 are still nearly just as slow as alloy A1 and A2, as their softenig curves are more linear on a logarithmic time scale, indicating more recovery. The classic drop in mechanical properties during recrystallization is not clearly observed, as recovery seems to be dominating. Maps from electron backscatter diffraction (EBSD) of the microstructure during softening shows that there are still nucleation and growth of recrystallized grains.
- The grain size prior to deformation is not of great importance to the softening kinetics, as little changes was observed by reducing the grain size from about 140 to 40 μm. The old grain boundaries may not be as important to nucleation as PSN, cube bands and transition bands in the particular alloys investigated.
- The recrystallized grain size is higher in alloy A1 and A2 than in alloy B1 and B2, most likely due to the higher amount of PSN sites. There somewhat higher grain growth in alloy A1 and A2 than in alloy B1 and B2 is probably due to slightly more solute drag, as concurrent precipitation is found to be low.
- The recrystallization texture consists of a mixture of the typical deformation components like S and copper and the typical recrystallization component cube. The cube orientation is slightly rotated around the normal direction, which supports that PSN is prevailed.
- No clear transition from recovery to recrystallization leads to difficulties when it comes to modelling, and it is difficult to use the classical recrystallization models like site saturation and Johnson Mehl. A time dependent nucleation model with a incubation time for start of recrystallization should be investigated further.

References

[1] G. I. Taylor, "The Formation of Emulsions in Definable Fields of Flow," *Royal Society of London Proceedings Series A*, vol. 146, pp. 501–523, Oct. 1934.

[2] K. Nord-Varhaug, B. Forbord, J. Benestad, T. Pettersen, B. Rønning, A. Bardal, S. Benum, K. Marthinsen, and E. Nes, "Substructure strengthening in aluminium alloys," in *Materials science forum*, vol. 331, pp. 1387–1392, Trans Tech Publ, 2000.

[3] F. Humphreys and M. Hatherly, *Recrystallization and related annealing phenomena*. Elsevier, 2004.

[4] C. Smith, "Grains, phases, and interfaces: As interpretation of microstructure," *MET TECHNOL*, vol. 15, no. 4, pp. 1–37, 1948.

[5] E. Hornbogen and U. Köster, *Recrystallization of Metallic Materials*. Rieder, 1978.

[6] J. Edgar, "Solubility of iron in solid aluminum," *Trans. AIME, l80*, pp. 225–229, 1949.

[7] M. Nishio, S. Nasu, and Y. Murakami, "Solid-solubility of iron in aluminium by means of the 57 fe mossbauer effect," *J JAPAN INST METALS*, vol. 34, no. 12, pp. 1173–1177, 1970.

[8] T. Furu, R. Ørsund, and E. Nes, "Subgrain growth in heavily deformed aluminium; experimental investigation and modelling treatment," *Acta Metallurgica et Materialia*, vol. 43, no. 6, pp. 2209 – 2232, 1995.

[9] K. Ito, R. Musick, and K. Lücke, "The influence of iron content and annealing temperature on the recrystallization textures of high-purity aluminium-iron alloys," *Acta Metallurgica*, vol. 31, no. 12, pp. 2137 – 2149, 1983.

[10] J. Murray and A. McAlister, "The al-si (aluminum-silicon) system," *Journal of Phase Equilibria*, vol. 5, pp. 74–84, 1984. 10.1007/BF02868729.

[11] R. Shoji and C. Fujikura, "Precipitation of Fe and Si in cold-rolled Al-Fe-Si sheet during annealing," *Key Engineering Materials*, vol. 44 and 45, pp. 163–180, 1990.

[12] H. Vatne, T. Furu, R. Ørsund, and E. Nes, "Modelling recrystallization after hot deformation of aluminium," *Acta Materialia*, vol. 44, no. 11, pp. 4463 – 4473, 1996.

[13] W. Johnson and R. Mehl, "Reaction kinetics in processes of nucleation and growth," *Trans. Aime*, vol. 135, no. 8, pp. 396–415, 1939.

[14] M. Avrami, "Kinetics of phase change. i general theory," *The Journal of Chemical Physics*, vol. 7, no. 12, pp. 1103–1112, 1939.

[15] A. Kolmogorov, "Statisticheskoi teori kristallizatsii metallov," *Izv. Akad. Nayuk CCCR*, vol. 2, pp. 355–359, 1937.

[16] J. Sæter, B. Forbord, H. Vatne, and E. Nes, "Modelling recovery and recrystallization, applied to back-annealing of aluminium sheet alloys," in *Proceedings of the 6th International Conference on Aluminium Alloys* (T. Sato, S. Kumai, T. Kobayashi, and Y. Murakam, eds.), vol. 1.

[17] P. A. Beck, "Annealing of cold worked metals," *Advances in Physics*, vol. 3, no. 11, pp. 245–324, 1954.

[18] F. Humphreys, "The nucleation of recrystallization at second phase particles in deformed aluminium," *Acta Metallurgica*, vol. 25, no. 11, pp. 1323 – 1344, 1977.

[19] O. Daaland, *Development of microstructure and texture during rolling and annealing of commercial Al-Mn-Mg alloys*. PhD thesis, NTNU, 1993.

[20] O. Daaland and E. Nes, "Recrystallization texture development in commercial Al-Mn-Mg alloys," *Acta Materialia*, vol. 44, no. 4, pp. 1413 – 1435, 1996.

[21] J. Burke, "Some factors affecting the rate of grain growth in metals," *AIME TRANS*, vol. 180, pp. 73–91, 1949.

[22] J. Burke and D. Turnbull, "Recrystallization and grain growth," *Progress in Metal Physics*, vol. 3, pp. 220–292, 1952.

[23] P. Gordon and T. El-Bassayouni, "The effect of purity on grain growth in aluminum," *Trans. AIMe*, vol. 233, pp. 391–397, 1965.

[24] O. ENGLER and J. HIRSCH, "Control of recrystallisation texture and texture-related properties in industrial production of aluminium sheet," *International journal of materials research*, vol. 100, no. 4, pp. 564–575, 2009.

[25] J. Hirsch and K. Lücke, *Acta Metall*, vol. 36, p. 2863. 1988.

[26] K. Lucke, "The orientation dependence of grain boundary motion and the formation of recrystallization textures," *Canadian Metallurgical Quarterly*, vol. 13, no. 1, pp. 261–274, 1974.

[27] J. Hirsch and K. Lücke, "The application of quantitative texture analysis for investigating continuous and discontinuous recrystallization processes of al-0.01 fe," *Acta Metallurgica*, vol. 33, no. 10, pp. 1927 – 1938, 1985.

[28] H. E. Vatne, O. Engler, and E. Nes, "Influence of particles on recrystallisation textures and microstructures of aluminium alloy 3103," *Materials Science and Technology*, vol. 13, no. 2, pp. 93–102, 1997-02-01T00:00:00.

[29] K. Lücke and O. Engler, "Effects of particles on development of microstructure and texture during rolling and recrystallisation in fcc alloys," *Materials Science and Technology*, vol. 6, no. 11, 1990.

[30] J. Hirsch in *7th Risø Symposium*, p. 349, 1986.

[31] O. Engler and M.-Y. Huh, "Evolution of the cube texture in high purity aluminum capacitor foils by continuous recrystallization and subsequent grain growth," *Materials Science and Engineering: A*, vol. 271, no. 1-2, pp. 371 – 381, 1999.

[32] H. Vatne, R. Shahani, and E. Nes, "Deformation of cube-oriented grains and formation of recrystallized cube grains in a hot deformed commercial almgmn aluminium alloy," *Acta Materialia*, vol. 44, no. 11, pp. 4447 – 4462, 1996.

[33] O. Engler, P. Wagner, D. Ponge, G. Gottstein, and J. Savoie, "Strain rate sensitivity of flow stress and its effect on hot rolling texture development," *Scripta Metallurgica et Materialia*, vol. 28:11, pp. 1317–1322, 1993.

[34] S. Panchanadeeswaran and D. Field, "Texture evolution during plane strain deformation of aluminum," *Acta Metallurgica et Materialia*, vol. 43, no. 4, pp. 1683 – 1692, 1995.

[35] D. Altenpohl, *Aluminium und Aluminiumlegierungen*. Springer-Verlag, 1965.

[36] Foerster, *Sigmatest 2.069 Operation Instructions*.

[37] "Tmt14 lecture notes," 2011.

[38] H. Bunge and P. Morris, *Texture analysis in materials science: mathematical methods*. Butterworths London, 1982.

[39] http://aluminium.matter.org.uk, 2012.

[40] S. Rodahl and Y. Li, "Investigations of alloys." Moreal meeting presentation, 10 2011.

[41] Y. Li and K. Marthinsen. personal communication, 2012.

[42] G. Abbruzzese and P. Brozzo, "Grain growth in polycrystalline materials," *Trans Tech Publications, Zurich*, 1992.

[43] C. Thompson and R. Carel, "Stress and grain growth in thin films," *Journal of the Mechanics and Physics of Solids*, vol. 44, no. 5, pp. 657–673, 1996.

[44] P. Beck and H. Hu, "Annealing textures in rolled face-centered cubic metals," *J. Metals (NY)*, vol. 4, 1952.

[45] T. Furu, *Modelling of recrystallization applied to commercial aluminium alloys*. PhD thesis, 1992.

[46] J. A. Sæter, *Substructure evolution and strengthening in cold rolled and annealed aluminium alloys*. PhD thesis, 1997.

[47] S. Tangen, *Deformation and annealing behavior of commercial non-heattreatable aluminium alloys*. PhD thesis, 2004.

[48] G. Sande, "Numerisk modellering av rekrystallisasjon i aluminiumslegeringer." TMT4500 Project work, December 2011.

A Grain size distributions

The complete grains size distributions, measured from the EBSD-maps, from the as-cast, homogenized and the annealed material is here presented graphically in Figure A.1-A.3.

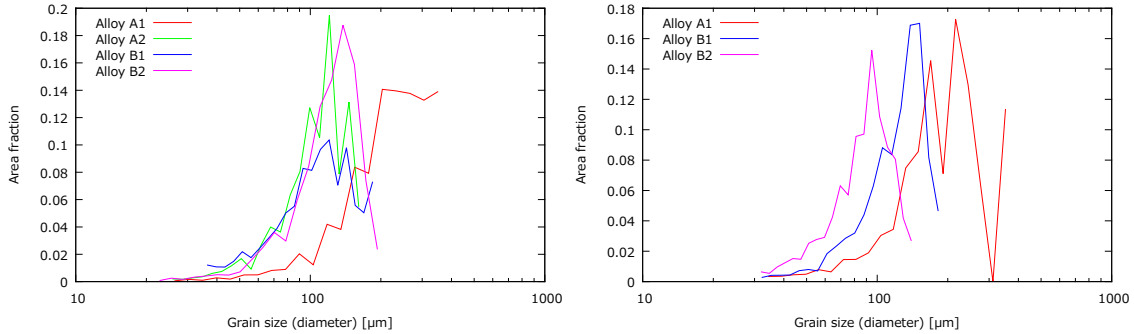

(a) As-cast material **(b) Homogenized material**

Figure A.1: Grain size distribution for the measurements of the as-cast and homogenized material.

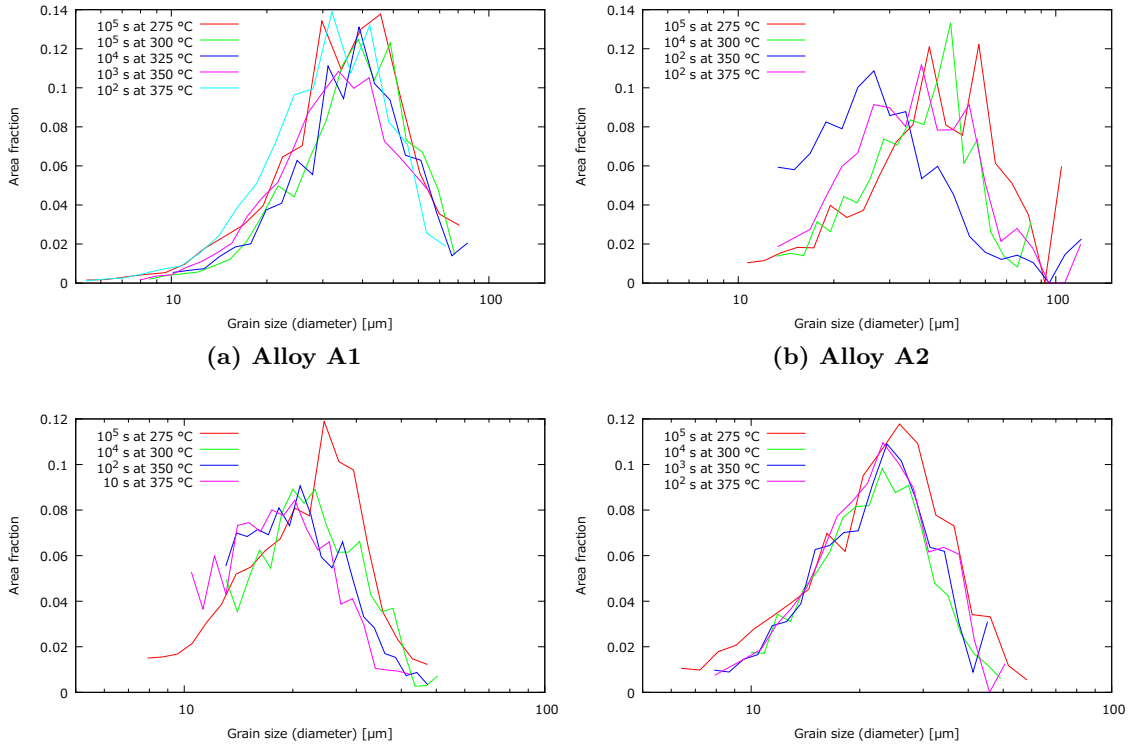

(a) Alloy A1 **(b) Alloy A2**

(c) Alloy B1 **(d) Alloy B2**

Figure A.2: Grain size distribution for the measurements of the recrystallized material.

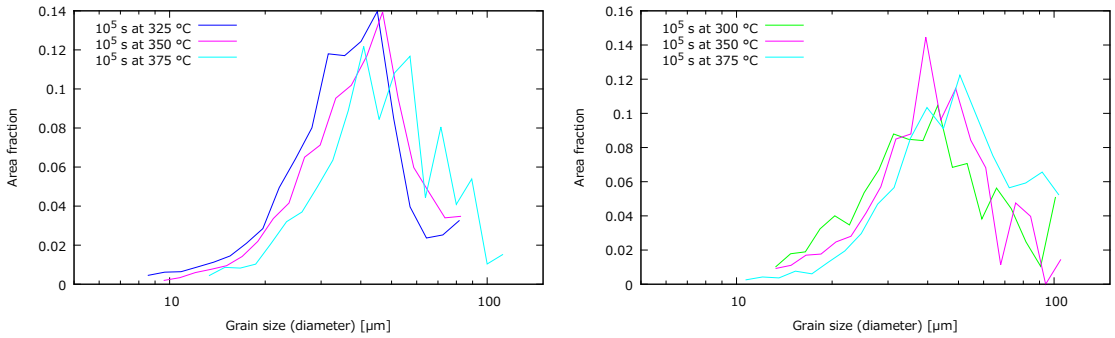

(a) Alloy A1

(b) Alloy A2

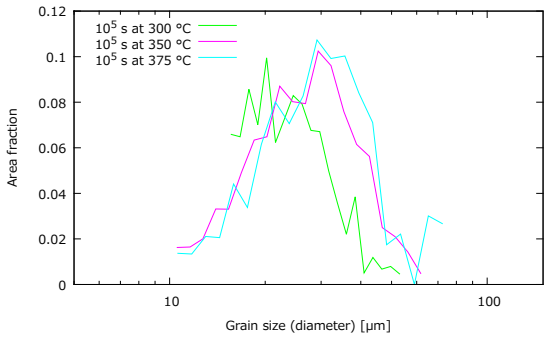

(c) Alloy B1

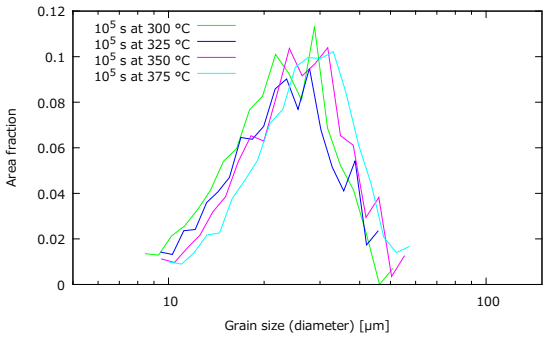

(d) Alloy B2

Figure A.3: Grain size distribution for the measurements of the recrystallized material used for grain growth.

B Homogenization temperature

During homogenization, the temperature was logged every 15 minutes with a Fluke 54II temperature logger. The temperature data is graphically given in Figure B.1.

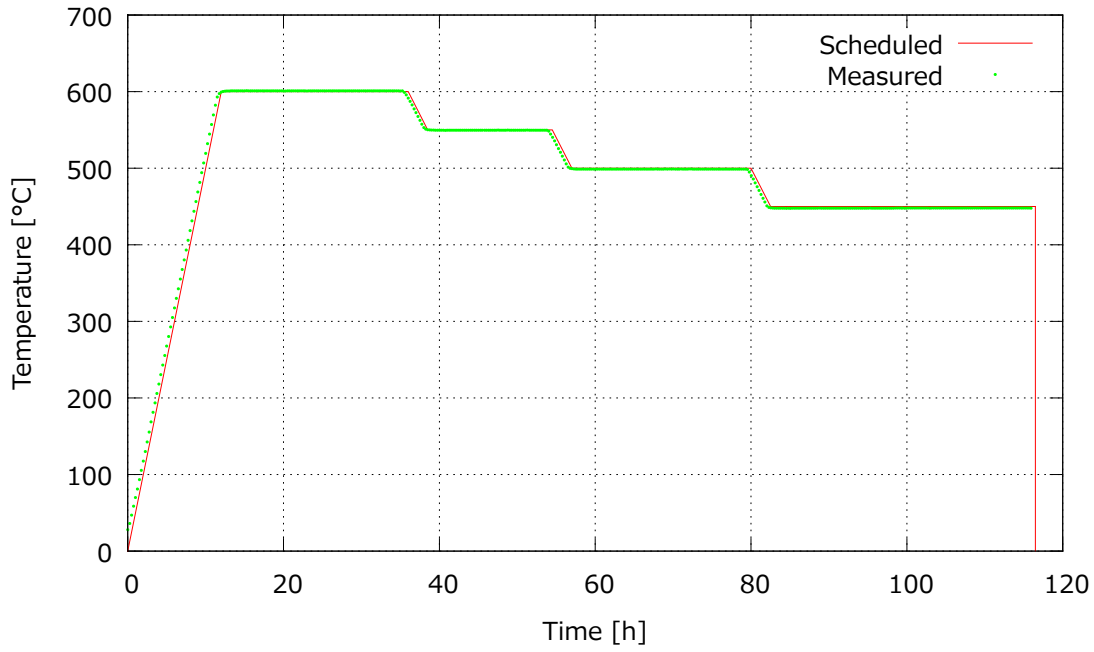

Figure B.1: The measured temperature during homogenization, logged with a Fluke 54II temperature logger.

C Alloy A1 with finer grain size

After the initial grain size in alloy A1 was reduced, the microstructure was characterized in EBSD. The

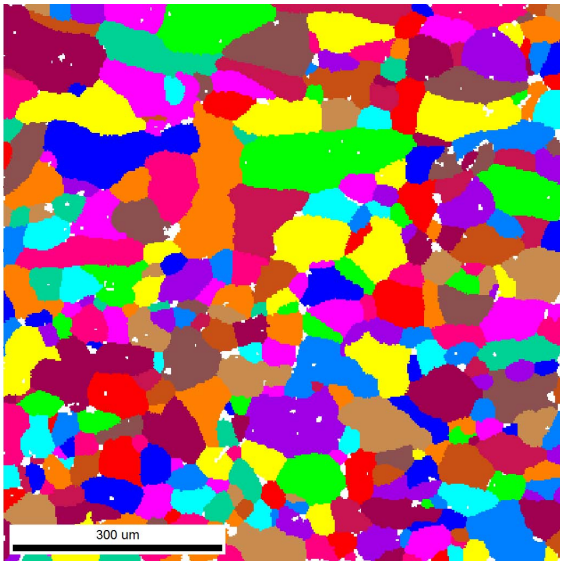

Figure C.1: Unique grain colour maps of alloy A1 before deformation from 100X EBSD-map.

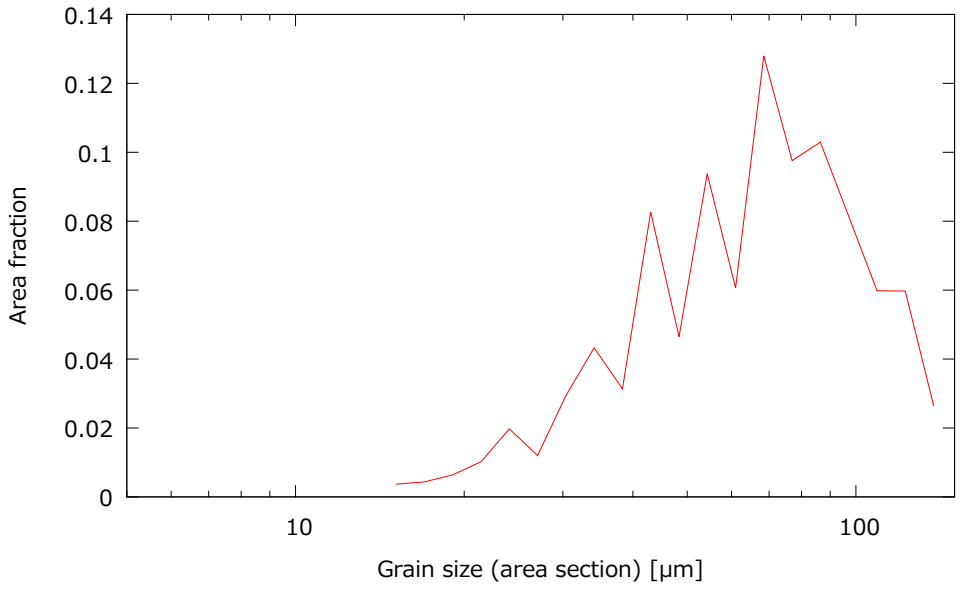

Figure C.2: Grain size distribution for the measurements of the alloy A1 with reduced grain size, prior to deformation.